Bioarchaeology International
Volume XX, Number XX: 1–23
DOI: 10.5744/bi.2022.0024

Assessing the Impact of Holocene Climate Change on Bioavailable Strontium Within the Nile River Valley

Geochemical and Radiogenic Isotope Perspectives

Antonio Simonetti,[a*] Michele R. Buzon,[b] Stefanie S. Simonetti,[a] Kari A. Guilbault,[b] Maha Ahmed Kordofani,[c] and Naomi F. Miller[d]

[a]Department of Civil and Environmental Engineering and Earth Sciences, University of Notre Dame, Notre Dame, Indiana 46556, USA
[b]Department of Anthropology, Purdue University, West Lafayette, Indiana 47909, USA
[c]Department of Botany, Faculty of Science, University of Khartoum, Sudan
[d]Near East Section, University of Pennsylvania Museum, Philadelphia, Pennsylvania 19104, USA

*Correspondence to: Antonio Simonetti, Department of Civil and Environmental Engineering and Earth Sciences University of Notre, 156 Fitzpatrick Hall, Notre Dame, Indiana 46556, USA
E-mail: simonetti.3@nd.edu

ABSTRACT The impact of the climate drying during the Holocene within the Nile River Valley System (NRVS) has been the focus of recent debate in the archaeological community. It is argued that the increased contribution of aeolian material from the neighboring Sahara Desert during the last ~7,000 years has changed the isotope compositions of bioavailable Sr relative to the geological background and thus hinders provenance investigations of human remains within the NRVS. This study reports new trace element and strontium (Sr), neodymium (Nd), and lead (Pb) isotope compositions for a combined total of 125 samples consisting of human tooth enamel and various faunal samples from different time periods, and present-day botanical samples from 11 archaeological sites along the NRVS. The new isotope data combined with published data do not support a time-dependent increase in a Saharan aeolian bioavailable Sr component during the Holocene within the NRVS; in general, Sr isotope compositions for human enamel samples match those of their corresponding faunal matrices, and these define a similar range of isotope compositions over the various time periods. The Nd and Pb isotope compositions for human tooth enamel reported here also support the limited contribution of Saharan aeolian dust within the NVRS.

Keywords: climate change; Holocene; Nile River Valley; Sr; Nd; and Pb isotope ratios

Ancient Residential Mobility – Nile River Valley System (NRVS)

The identification of residential mobility of past human groups via strontium isotope analysis ($^{87}Sr/^{86}Sr$ compositions) has been successfully used by researchers in long-term, multidimensional investigations of population composition and dynamics with a contextual bioarchaeological approach in many regions (e.g., Buzon et al. 2016; Evans et al. 2006; Turner et al. 2009). For example, the Nile River Valley System (NRVS) has been viewed as a corridor or "interactive highway" (Graves 2018) in northeast Africa; beginning in about 3000 B.C., people living in Nubia and Egypt regularly

Received 10 August 2022
Revised 25 January 2023
Accepted 25 January 2023

interacted, traveling up and down the Nile as well as the desert regions to the east and west. Buzon and colleagues (2016) investigated the population dynamics and cultural transformations at the site of Tombos (Fig. 1), the frontier zone of ancient Nubia and Egypt during a period of rapid governmental transition from Egyptian colony to independent Nubian Napatan state (ca. 1400–650 B.C.).

Higher $^{87}Sr/^{86}Sr$ values at Tombos have been associated with the presence of non-locals during the Egyptian colonial period (Buzon et al. 2007). Recently, an alternative explanation has been suggested: The higher values are due to greater quantities of aeolian material in the windblown dust being incorporated into farmed alluvial deposits (Woodward et al. 2015). This study evaluates the hypothesis that Sr isotope compositions have been altered over time due to the processes associated with climate change during the Holocene through trace element and Sr, Nd, and Pb isotope compositions for 125 new samples of archaeological human and faunal tooth enamel, and present-day plant samples growing on or near 11 archaeological sites along the NRVS.

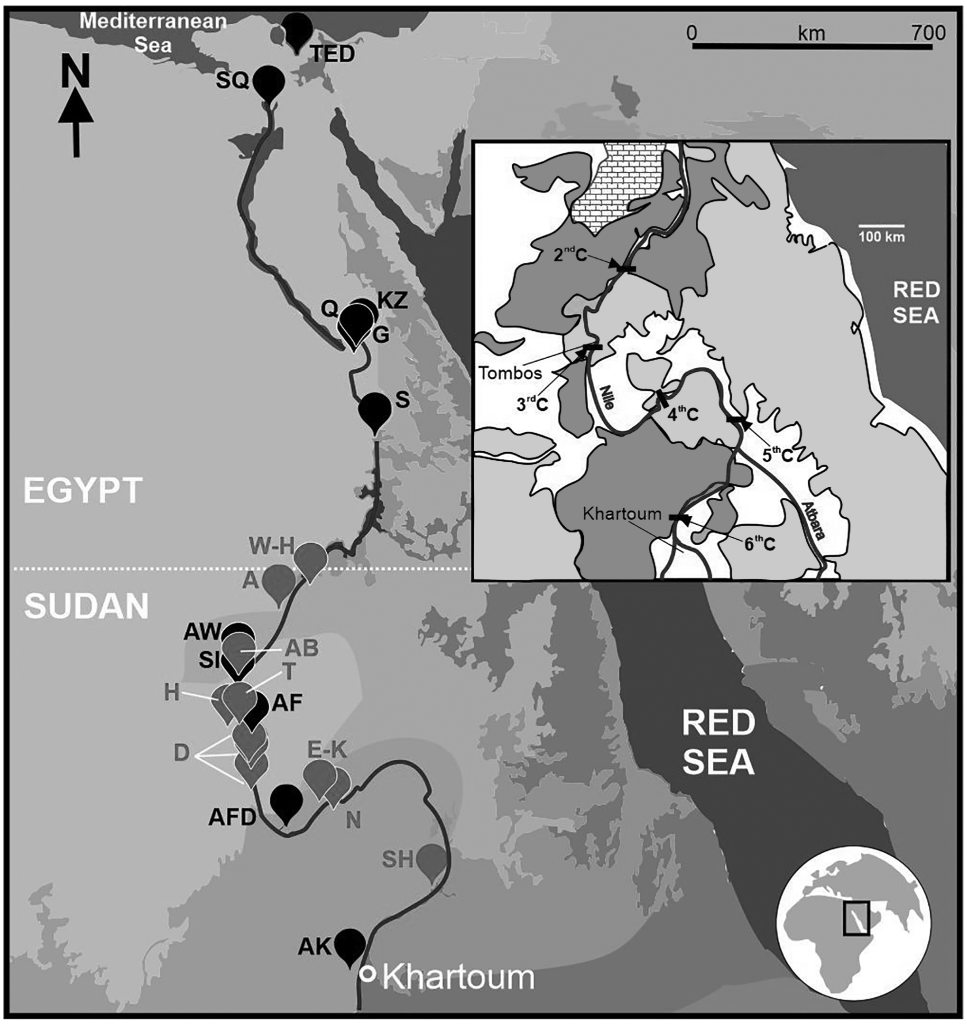

Figure 1. Modified Google Earth map showing the locations of the archaeological burial sites investigated here (non-black font) within the Nile River Valley System (NRVS) in northeastern Africa (*bottom right inset*). Sites labeled in black font represent those with Sr isotope compositions from literature data included in the compilation illustrated in Fig. 7. The letter abbreviations correspond to the following burial sites: **A** = Askut; **AB** = Abri; **AF** = Abu Fatima; **AFD** = Afad; **AK** = Al-Khiday; **AW** = Amara West; **D** = Dongola sites (El-Detti, Selib Bahri, Selib 1); **E-K** = El-Kurru; **G** = Gournah; **H** = Hannek; **KZ** = Khozan; **N** = Nuri; **Q** = Qurneh; **S** = Shellal; **SH** = Shendi/Meroe; **SI** = Sai Island; **SQ** = Saqqara; **T** = Tombos; **TED** = Tell el-Dab'a; **W-H** = Wadi Halfa. *Top right inset*: Regional geological sketch map modified from Padoan and colleagues (2011). Lighter shaded areas = Precambrian basement rocks of the Saharan Metacraton (SMC) and Arabian Nubian Shield (ANS), darker shaded areas = Mesozoic sedimentary deposits (mainly sandstone), brick pattern = Paleogene limestone deposits, and areas in white represent regions covered in unconsolidated alluvium deposits. Locations of Cataracts numbers 2 to 6 are also shown.

Strontium isotope Geochemistry and its Bioavailability

On Earth, the $^{87}Sr/^{86}Sr$ ratios of geological materials are dependent on their age and mineralogical make-up, which is a function of the geological composition of their place of origin (Faure 1986). Areas that are characterized by older bedrock with a higher proportion of minerals containing high Rb/Sr ratios, such as micas (e.g., biotite, muscovite, alkali feldspar), yield higher $^{87}Sr/^{86}Sr$ ratios than those in regions that contain younger rocks with lower Rb/Sr ratios (Faure 1986). Over time, the parent nuclide ^{87}Rb decays to the stable daughter isotope ^{87}Sr via beta decay (half-life of ~50 billion years; Faure and Mensing 2005). The $^{87}Sr/^{86}Sr$ signatures are then transferred into the hydrosphere and biosphere through weathering. Animals record the $^{87}Sr/^{86}Sr$ compositions of their environment and diet, and this signature is incorporated into their body tissues, mainly skeletal hydroxyapatite, substituting for Ca (Ericson 1985; Nelson et al. 1986). Tissues that grow continuously, such as hair (Shin et al. 2022), teeth (Lahtinen et al. 2021), bones (Tütken et al. 2011), and tusks (Barbieri et al. 2008), may record temporal variations in the $^{87}Sr/^{86}Sr$ ratios (Hillson 1996), which can then be used to decipher migration patterns of individuals or groups from ancient civilizations (Buzon et al. 2007; Buzon and Simonetti 2013; Buzon et al. 2016).

Although Sr found within bedrock is the ultimate source of Sr to Earth surface systems, its $^{87}Sr/^{86}Sr$ signature can differ significantly from that of soils, surface water, and organisms due to many features at the local scale, such as variation in weathering rates for different minerals, the local soil pH, animal behavior, or possible input from aeolian sources (Bentley 2006; Capo et al. 1998; Chadwick et al. 1999; Stewart et al. 1998). For provenance investigations, it is most appropriate to model the "biologically available Sr" as an approximation of the Sr that is incorporated by organisms (Frei and Frei 2011; Hodell et al. 2004; Price et al. 2002; Sillen et al. 1998).

Nile River Valley System (NRVS)—Geological Background

The bedrock and alluvium deposits that are present within and that surround the NRVS are varied and include the following predominant geologic regions: volcanic Ethiopian Highlands, Precambrian basement rocks of the Arabian Nubian Shield (ANS) and Saharan Metacraton (SMC), and Phanerozoic sedimentary cover (Fig.1). In northern Ethiopia and Yemen, Oligocene-aged (~30 million years ago) volcanism resulted in the emplacement of thick continental flood basaltic sequences that directly overlie Pan-African basement rocks (Pik et al. 1999). Crystalline basement rocks (between ~1000 and ~600 million years old) present within the ANS are interpreted as newly formed Neoproterozoic crust and represent dismembered ophiolite (Abdel-Rahman 1993; Abdelsalam et al. 1998). The ANS comprises metasedimentary rocks with marine protoliths, arc-related metavolcanic rocks and (meta)intrusions of intermediate to granitoid composition (Bailo et al. 2003; Barth and Meinhold 1979; Evuk et al. 2014 and references therein; Küster et al. 2008). In contrast, units from the SMC represent older cratonic crust that was deformed during the Neoproterozoic (between ~1000 and ~550 million years old) and consist of polymetamorphic amphibolite from magmatic arc environments (e.g., Küster and Liégeois 2001). The rock types present within the SMC comprise mainly felsic medium- to high-grade polymetamorphic granitoids, including meta-granite and rare meta-monzonite (Barth and Meinhold 1979; Küster et al. 2008; Evuk et al. 2014 and references therein).

Subsequent to the tectonically active and orogenic periods associated with the SMC and ANS, much of the region now occupied by the NRVS was characterized by prolonged intervals of erosion and continental sedimentation leading to widespread accumulation of sandstones (e.g., Mesozoic Nubian sandstone formation; Williams 2019). In the northern areas of the NRVS, the regional geology is dominated by Cenozoic sedimentary rock formations (Dakhla chalk, Esna shale, and Theban limestone) deposited between 35 and 56 Ma ago (Fig. 1). Moreover, at Luxor (ancient Thebes), the Theban limestone formation is ~300 meters thick and underlain by the Esna shale (60 meters thick; Said 1962).

Given the varied geological background described above, the total range of Sr and Nd isotope compositions within a particular region may be significant; however, the overall range of $^{87}Sr/^{86}Sr$ and ε_{Nd} values, respectively within the NVRS are as follows: Ethiopian basalts: 0.7030 to 0.7043 and +7 to −1 ‰ (Pik et al. 1999); ANS-SMC Precambrian basement: 0.7032 to 0.7089 and +8 to −4 ‰ (Evuk et al. 2017); and Cenozoic marine deposits: 0.7090 to 0.7092 (Reinhardt et al. 1998). As shown and discussed later, these Sr and Nd isotope compositions exhibit minimal overlap with those for human enamel, faunal, and botanical samples from archaeological sites investigated here.

Temporal Variability of Bioavailable Sr, Pb, Nd: Impact of Holocene Climate Change?

Previous investigations have not given much attention to the supply of sediment from windblown or aeolian

—-1
—0
—+1

dust and the numerous wadis in Sudan and Egypt (aeolian source) to the NRVS between Khartoum and the Mediterranean Sea (~2700 km in length; Fig. 1). Paleo-dust records worldwide show that wind-borne mineral aerosol or dust is strongly linked with climate state (Maher et al. 2010). For example, previous investigations indicate that concentrations of dust in sediments and ice cores have varied greatly in association with transitions from glacial to interglacial regimes; during glacial stages, Earth was significantly dustier, with dust fluxes two to five times greater than in interglacial stages (Kohfeld and Harrison 2001). The generation and transport of dust is itself extremely sensitive to climate, with aridity being the most obvious link since the dominant sources of dust globally are all located in arid or semiarid regions (Maher et al. 2010). Dust production is a highly complex process that depends on many factors, such as atmospheric, soil, and terrain properties (Goudie 2008). Consequently, sediment detachment from the surface and transport is mostly associated with strong winds; however, particle detachment is constrained by several factors with soil moisture playing a vital role since it affects particle cohesion along with cementation as a function of salt content and soil structure (Maher et al. 2010). Therefore, dust emission is higher in arid or semiarid areas, such as deserts with annual rainfall of less than ~25 cm per year (Prospero et al. 2002; Washington et al. 2003), little or no vegetation cover, and strong, long-fetch winds.

It is well established that the Sahara is the largest source of mineral dust on Earth (Goudie 1983), in particular the Bodélé Depression, which is located in Chad, southeastern Sahara (Goudie and Middleton 2001). This region is characterized by the accumulation of dust and a predominance of fine material due to the arid conditions and resulting from the sedimentation of diatomites during the early phases of the drying of the paleo-lake "Mega-Chad" (Washington et al. 2003). Hence, the hypothesis was proposed that dust from the neighboring Sahara has overprinted the Sr isotope anthropological record in the NRVS, in particular during the drying climate of the Holocene period. Woodward and colleagues (2015) published Sr and Nd isotope data for dated floodplain deposits in the Desert Nile with the goal of reconstructing long-term shifts in the catchment sediment sources of the Nile. Their results indicate that the sediment load of the Nile has been dominated by input from the Ethiopian Highlands for much of the Holocene; however, tributary wadis and aeolian sediments have had a major impact on the valley floor sedimentation. Thus, it is argued that global climate change throughout the Holocene influenced Nile Valley drainage, and hence impacted the temporal strontium isotope signatures and bioarchaeological approaches that assess population mobility using this method. They contend that aeolian wind-borne dust may have been ingested by Egyptians and Nubians, which may have resulted in a progressive increase in their $^{87}Sr/^{86}Sr$ values. Moreover, Woodward and colleagues (2015) suggested that the extensive dental wear present in Nile Valley populations (Buzon and Bombak, 2010) corroborates their hypothesis.

In a recent study by Schrader and colleagues (2019), however, comparison of Sr isotope signatures for one Upper Nubian region in the NRVS do not show chronological strontium variability from the earlier samples (Kerma-period Abu Fatima) to the later samples (New Kingdom Hannek and Tombos; see Table S2 for regional chronology). Based on the available data, Schrader and colleagues (2019) concluded that the Abu Fatima and Tombos Sr isotope signals overlap. If an increasing contribution of aeolian sediments over time did indeed occur, then one would expect to find higher Sr isotope ratios in younger archaeological samples. In contrast, Buzon and colleagues (2016) found quite the opposite: $^{87}Sr/^{86}Sr$ ratios in skeletal material dating to the New Kingdom period (1500–1070 B.C.), including the multiple hypothesized migrants, was higher ($n = 55$, $\bar{x} = 0.70780$, 0.70712-0.70935, $SD = 0.0005$) than the later Third Intermediate/Napatan Period (1070–650 B.C.; $n = 30$, $\bar{x} = 0.70749$, 0.70661-0.70789, $SD = 0.0003$). For these reasons, the hypothesis that the Sr isotope signatures of human remains from the NRVS have been impacted by Holocene climate change, in particular those that have been recorded in the areas between the Second and Third Cataracts within the last ~2,000 years, is somewhat doubtful.

Thus, this study investigates the climate change hypothesis using a multi-pronged research approach: (1) Report additional Sr isotope analyses of faunal and soil samples and for remains of humans with well characterized age of death; these are compared to their present-day equivalents to develop a more detailed temporal evolution/stratigraphy of the bioavailable Sr isotope signature in the NRVS; and (2) determine trace element and Nd, Pb, and Sr isotope signatures of botanical samples within different regions of the NRVS in order to better assess the modern-day isotope signature of bioavailable Sr in this part of the globe. This will allow us to better evaluate the possible impact of aeolian/wind-borne contribution during the Holocene.

Plants incorporate the bioavailable Sr present in the local soil for any given region, which is derived from both geological weathering of local bedrock and atmospheric input (Graustein and Armstrong 1983; Miller et al. 1993; Probst et al. 2000; Vitousek et al. 1999; Whipkey et al. 2000). Atmospheric sources predominate only if the rate of aeolian deposition of bioavailable Sr is greater than that of bedrock weathering (Hodell et al. 2004). The relative contribution of atmospheric Sr versus that of local bedrock weathering increases as the age of the rock increases, a feature that has been well documented in volcanic soils of different ages and the plants that grow on them in Hawaii (Chadwick et al. 1999; Kennedy et al. 1998; Stewart et al. 1998; Vitousek et al. 1999). This time-dependent process of atmospheric bioavailable Sr accumulation may be evaluated by comparing $^{87}Sr/^{86}Sr$ compositions in plants with different root systems, which varies in response to water availability and plant growth (Canadell et al. 1996). For example, a global survey of plant rooting depths indicates that 44% of grass roots are concentrated in the top 10 cm of soil, compared with 21% in shrubs (Jackson et al. 1996). Hence, it is generally assumed that the contribution of bioavailable atmospheric Sr gradually decreases with soil depth (Capo et al. 1998; Vitousek et al. 1999). Lastly, (3) combine the new $^{87}Sr/^{86}Sr$ isotope data with isotope compositions of Pb and Nd for the samples investigated here; the latter two isotope systems provide additional insights into provenance (Evans et al. 2018; Plomp et al. 2019) and possible effects of climate change within the NRVS.

Lead ingested by modern-day humans is predominantly from two sources: natural (soil-derived) and anthropogenic (modern human industrial activities); the latter is obviously not significant for this study. Exposure to natural Pb from soil results in variable abundances and isotope ratios in teeth that depend on the local geology, but Pb levels are generally low (~0.5–0.7 ppm; Montgomery et al. 2010; Millard et al. 2014). As with Sr and Pb, Nd and its isotope ratios are transferred from rocks to the vegetation and bodies of water, entering the human body through primarily diet (Kamenov et al. 2018; Pietra et al. 1985; Plomp et al. 2017). Nd isotopes do not fractionate during their uptake by the human body, and therefore reflect those of the food, water, and dust consumed (Pye, 2004; Tütken et al. 2011). To date, previous studies investigating the role of Nd in biological systems are scarce (Plomp et al. 2019) due to the relatively low concentrations of Nd present in human tissues (< 0.7 ppm), and dental enamel (0.1 to 58.0 ppb; Kamenov et al. 2018; Plomp et al. 2017), which may hinder its use in provenance studies. As summarized by Plomp and colleagues (2019), the low abundances of Nd in human tissues may be attributed to (1) the scarcity of Nd in the food chain (ppb range; Goldstein and Jacobsen 1987; Tyler 2004; Kulaksiz and Bau 2013), (2) the lack of physiological or biological function of Nd in the human body (Evans 1990), and (3) the incompatible nature of the trivalent ion (Nd^{3+}) substitution for calcium (Ca^{2+}) in the crystal lattice of human bone and teeth (Evans 1990; Plomp et al. 2017).

Samples

Assessing the temporal variability of bioavailable Sr for the NRVS includes available $^{87}Sr/^{86}Sr$ compositions, such as results for the 250 specimens reported in Buzon and Simonetti (2013), which consist of both archaeological human (n = 189) and faunal samples (n = 61). Tables 1 and 2 list all of the new trace element and isotope results for specimens investigated here, which include various modern-day plants (N = 40, Table 1), soil (N = 3), faunal (N = 27), foraging animals such as sheep, goat, hare, pig, and human (N = 55, tooth enamel) samples; detailed descriptions for human enamel and faunal samples are listed in Supplementary Information Table S1. Plant samples from Tombos, Abri, and Wadi Halfa were collected by Michele Buzon, samples from El-Kurru were collected by Naomi Miller, and Dongola plants were collected by Iwona Kozieradzka-Ogunmakin. Plant identification was completed by Naomi Miller and Maha Kordofani. Abagail Breidenstein contributed human and faunal enamel samples from the El-Kurru (with Geoff Emberling) and Nuri (with Pearce Paul Creasman) projects. El Detti (Polish Centre of Mediterranean Archaeology, Mahmoud El-Tayeb), SRAP (Shendi, National Corporation for Antiquities and Museums), Selib 1, and Selib Bahri (Institute of Mediterranean and Oriental Cultures, Polish Academy of Science, Bogdan Zurawski) samples were contributed by Iwona Kozieradzka-Ogunmakin. Tombos human and faunal remains were contributed by Michele Buzon (with Stuart Tyson Smith). Askut faunal remains were samples from the Fowler Museum at the University of California, Los Angeles (facilitated by Shayla Monroe and Stuart Tyson Smith). The ages of archaeological samples investigated here have been assigned based on a chronology adapted from Smith (1998) and are listed in Supplementary Information Table S2.

Modern botanical and enamel samples

In this study, we have adopted the plant rooting system reported by Wong and colleagues (2021), which identifies plants as having shallow (grass), medium (bush or shrub), or deep root (tree) systems (Table 1); the leaves of herbaceous plants, including grasses, were preferentially sampled. All modern botanical samples collected in the field were dried on site in order to avoid sample degradation subsequent to collection and prior to analysis.

Enamel samples investigated here were mechanically cleaned and abraded as well as chemically purified to reduce post-depositional contamination (Nielsen-Marsh and Hedges 2000). The abundances of trace elements (Mg, V, Mn, Fe, Cu, Zn, Sr, Ba, Nd, Pb, and U)

Table 1. Descriptions of botanical samples investigated here.

Sample	Root Category	Location	Identification
TOP-1	Deep	Tombos	*Azadirachta indica* A. Juss.
TOP-2	Deep	Tombos	*Conocarpus erectus* L.
TOP-3	Deep	Tombos	*Phoenix dactylifera* L.
TOP-4	Shallow	Tombos	*Cymbopogon schoenanthus* (L.) Spreng.
TOP-6	Medium	Tombos	*Pulicaria undulata* (L.) C.A. Mey. subsp. *undulata*
TOP-7	Shallow	Tombos	*Trifolium dubium* Sibth.
TOP-8	Medium	Tombos	*Pulicaria undulata* (L.) C.A. Mey.
TOP-9	Medium	Tombos	*Aerva javanica* (Burm.f.) Juss. ex Schult.
TOP-10	Medium	Tombos	*Tamarix nilotica* (Ehrenb.) Bunge
TOP-11	Medium	Tombos	*Rhynchosia minima* (L.) DC. var. *minima*
ABR-1	Deep	Abri	*Eucalyptus microtheca* F. Muell.
ABR-2	Deep	Abri	*Azadirachta indica* A. Juss.
ABR-3	Deep	Abri	*Acacia senegal* (L.) Willd. var. *senegal*
WH-1	Medium	Wadi Halfa	*Fagonia cretica* L.
WH-3	Medium	Wadi Halfa	*Tamarix nilotica* (Ehrenb.) Bunge
WH-4	Medium	Wadi Halfa	*Pulicaria undulata* (L.) C.A. Mey. subsp. *undulata*
WH-5	Shallow	Wadi Halfa	*Echinochloa colona* (L.) Link
WH-6	Shallow	Wadi Halfa	*Sonchus oleraceus* L.
WH-7	Deep	Wadi Halfa	*Phoenix dactylifera* L.
WH-8	Deep	Wadi Halfa	*Citrus limon* (L.) Burm.
WH-9	Medium	Wadi Halfa	*Phragmites australis* (Cav.) Trin. ex Steud. subsp. *altissimus* (Benth.) Clayton
WH-10	Deep	Wadi Halfa	*Azadirachta indica* A. Juss.
DON-1	Medium	Dongola	*Ambrosia dumosa* (A. Gray) W.W. Payne
DON-2	Medium	Dongola	*Aerva javanica* (Burm.f.) Juss. ex Schult.
DON-3	Medium	Dongola	*Calotropis procera* (Aiton) W.T. Aiton.
KUP-1	Deep	El-Kurru	*Balanites aegyptiaca* (L.) Delile var. *aegyptiaca*
KUP-2	Deep	El-Kurru	*Phoenix dactylifera* L.
KUP-3	Deep	El-Kurru	*Acacia ehrenbergiana* Hayne
KUP-4	Deep	El-Kurru	*Maerua crassifolia* Forssk.
KUP-5	Deep	El-Kurru	*Acacia nilotica* (L.) Willd. ex Delile subsp.*nilotica*
KUP-6	Medium	El-Kurru	Fabaceae indet.
KUP-7	Medium	El-Kurru	*Senecio*
KUP-8	Medium	El-Kurru	Amaranthaceae
KUP-9	Medium	El-Kurru	*Citrullus colocynthis* (L.) Schrad.
KUP-10	Medium	El-Kurru	*Chenopodium album* L.
KUP-11	Shallow	El-Kurru	Poaceae
KUP-12	Deep	El-Kurru	*Ziziphus spina-christi* (L.) Desf.
KUP-13	Shallow	El-Kurru	*Echinochloa colona* (L.) Link
KUP-14	Shallow	El-Kurru	*Setaria verticillata* (L.) P. Beauv.
KUP-15	Shallow	El-Kurru	*Cynodon dactylon* (L.) Pers.

for the samples examined here were determined in order to assess the degree of post-mortem diagenetic alteration (Hedges and Millard 1995; Kohn et al. 1999). Moreover, the abundances of the trace elements (C) obtained here (Table 2) are compared to their respective established maximum threshold concentrations (MTC) for archaeological tooth enamel as defined by Kamenov and colleagues (2018). Naturally, using calculated MTC values, which equate to the addition of the maximum concentrations plus two times the standard deviation for concentrations in modern samples, evaluation of diagenetic alteration is not a 100% foolproof method, especially since MTC values were established based on a single archaeological population (Kamenov et al. 2018). For example, a more robust approach would entail using a combination of both trace element abundances and Pb isotope ratios, such as Simonetti and colleagues (2021) recently demonstrated for tooth enamel from human remains at El-Kurru, Sudan. In this study, a vast majority of samples yield C/MTC values for most elements ≤1 and are thus deemed non-altered and equivalent to modern-day tooth enamel (i.e., *in vivo*; Kamenov et al., 2018), the exception being C/MTC values for V, Fe, and Nd (Fig. 2). Samples of enamel characterized by C/MTC values > 1.0 for Fe and Nd combined with anomalous ε_{Nd} values (i.e., those that are distinct from either the main group of remaining enamel and/or faunal samples from the same region are considered suspect and therefore excluded from diachronic comparison). As for the Pb isotope ratios (Table 3; Figs. 5 and 6), enamel samples that plot along a mixing line involving radiogenic Pb (derived from U-rich groundwater endmember) as demonstrated by Simonetti and colleagues (2021) are also excluded from the diachronic comparison. Thus, the following individual enamel samples have also been excluded (five in total) for provenance purposes: from the Dongola region (samples Seb-1, -11, and Det-1) and from the Shendi region (samples Sra-2, and -3).

Table 2. Trace element concentrations (ppm) of samples in this study. The 2σ level relative standard deviation (RSD% = standard deviation/average concentration × 2 × 100) is a function of absolute elemental concentration, and thus varies between ~2.5 and ~6.0% for the more abundant elements (Mg, Mn, Fe, Sr, Ba) and between ~15 and ~46% for Nd, Pb, and U (≪ 1 ppm). n.a. = not analyzed. H = human, V = botanical samples (vegetation), F = faunal, S = soil; b.d.l. = below detection limit.

Sample	Type	Date	Mg	V	Mn	Fe	Cu	Zn	Sr	Ba	Nd	Pb	U
El-Kurru													
KUR-1	H	Christian	2276	n.a.	3.53	286	n.a.	n.a.	188	10.5	0.07	0.16	0.18
KUR-2	H	Christian	2148	n.a.	21.5	436	n.a.	n.a.	245	35.6	0.19	1.28	0.30
KUR-3	H	Christian	2215	n.a.	34.3	400	n.a.	n.a.	343	79.9	0.38	9.58	1.52
KUR-4	H	Christian	2289	n.a.	2.52	302	n.a.	n.a.	172	5.80	0.13	0.11	0.07
KUR-5	H	Christian	973	n.a.	11.8	141	n.a.	n.a.	106	18.7	0.06	0.23	0.20
KUR-6	H	Christian	2627	n.a.	13.0	325	n.a.	n.a.	221	16.5	0.09	0.71	0.16
KUR-7	H	Christian	2942	n.a.	13.9	565	n.a.	n.a.	398	52.1	0.35	0.85	0.21
KUR-8	H	Christian	2513	n.a.	20.2	352	n.a.	n.a.	188	19.4	1.15	0.33	0.08
KUR-9	H	Christian	2605	n.a.	7.09	338	n.a.	n.a.	256	36.1	0.18	0.43	0.42
KUR-10	H	Christian	3181	n.a.	8.35	391	n.a.	n.a.	236	26.8	0.28	0.97	0.32
KUR-11	H	Christian	2629	n.a.	41.8	509	n.a.	n.a.	225	15.0	0.50	62.0	0.34
KUR-12	H	Christian	2675	n.a.	29.2	368	n.a.	n.a.	291	80.9	0.38	22.5	1.30
KUR-13	H	Christian	2507	n.a.	9.09	317	n.a.	n.a.	115	9.94	0.90	3.17	0.12
KUR-14	H	Christian	2485	n.a.	17.2	369	n.a.	n.a.	425	73.0	0.22	0.63	0.47
KUR-15	H	Christian	2695	n.a.	41.2	393	n.a.	n.a.	286	25.4	0.76	0.29	0.35
KUR-16	H	Christian	2537	n.a.	66.2	440	n.a.	n.a.	290	81.9	0.32	2.89	1.40
KUR-17	H	Christian	2621	n.a.	9.26	278	n.a.	n.a.	181	14.3	0.10	2.60	0.11
KUR-18	H	Christian	2256	n.a.	23.8	322	n.a.	n.a.	169	33.4	0.31	7.73	0.71
KUP-1	V	P.D.	4614	0.58	54.3	267	8.87	30.0	96.8	8.60	0.20	0.14	0.27
KUP-2	V	P.D.	1614	0.38	21.2	141	1.44	22.2	23.8	4.35	0.12	0.09	0.10
KUP-3	V	P.D.	1467	1.53	28.9	649	5.12	30.9	96.3	5.30	0.47	0.49	0.03
KUP-4	V	P.D.	13868	3.92	113	1539	4.68	21.7	295	16.4	1.31	0.48	0.04
KUP-5	V	P.D.	1590	0.62	59.7	326	7.40	27.4	61.4	8.97	0.14	0.09	b.d.l.
KUP-6	V	P.D.	4964	1.12	196	647	8.87	35.7	235	24.3	0.43	0.18	0.10
KUP-7	V	P.D.	1754	1.46	31.4	571	4.20	36.0	38.8	6.56	0.38	0.15	b.d.l.
KUP-8	V	P.D.	14936	2.10	67.8	817	5.59	18.2	37.6	5.71	0.52	0.23	b.d.l.
KUP-9	V	P.D.	13844	1.24	103	490	6.10	89.3	342	48.5	0.39	0.21	0.01
KUP-10	V	P.D.	11363	1.62	111	630	13.5	32.7	61.1	11.1	0.40	0.17	0.53
KUP-11	V	P.D.	2319	1.92	168	705	5.05	36.5	43.1	27.8	0.44	0.29	0.01
KUP-12	V	P.D.	4310	2.56	443	1315	8.91	49.2	173	42.6	0.56	0.42	0.01
KUP-13	V	P.D.	5027	1.73	282	735	10.3	55.9	50.4	20.5	0.42	0.15	0.04
KUP-14	V	P.D.	7735	5.83	438	2130	9.74	32.9	93.4	18.0	1.23	0.51	0.07
KUP-15	V	P.D.	1950	1.18	64.6	410	7.64	33.9	30.4	34.8	0.31	0.18	b.d.l.
Nuri													
NUF-1	F	Meriotic	41.0	0.26	8.67	134	0.38	b.d.l.	62.5	33.0	0.04	0.02	0.003
NUF-2	F	Meriotic	309	0.85	2.06	124	0.09	3.78	38.4	9.69	0.05	0.02	0.011
NUF-3	F	Meriotic	24.4	0.23	14.7	146	0.06	b.d.l.	3.52	3.80	0.03	0.02	0.003
NUF-4	F	Meriotic	863	1.71	11.9	483	0.58	11.5	154	31.2	0.35	0.13	0.039
NUF-5	F	Meriotic	1686	0.43	2.47	173	0.13	13.6	162	12.3	0.05	0.03	0.005
NSO-1	S	P.D.	13989	160	768	49820	39.3	138	419	600	27.3	10.6	1.77
Tombos & Hannek													
TOM-196	H	3rd Int. P.	4372	0.05	1.83	202	0.24	133	121	1.88	0.02	0.06	b.d.l.
TOM-197	H	3rd Int. P.	2753	0.12	3.55	247	0.23	178	177	2.06	0.05	0.03	0.01
TOM-198	H	3rd Int. P.	4227	0.08	1.86	217	0.39	150	101	1.74	0.01	0.12	b.d.l.
TOM-199	H	3rd Int. P.	4571	0.10	15.3	225	0.24	157	153	3.94	0.03	0.06	b.d.l.
TOM-200	H	3rd Int. P.	2369	3.52	25.1	2071	1.64	142	115	6.37	1.06	0.30	0.03
TOM-201	H	3rd Int. P.	2007	0.26	9.50	232	0.22	217	337	3.99	0.05	0.09	b.d.l.
TOM-202	H	3rd Int. P.	3929	0.41	22.3	267	0.33	185	180	4.43	0.06	0.07	b.d.l.
TOM-203	H	3rd Int. P.	2463	0.02	1.72	261	0.20	176	168	1.13	0.14	0.08	b.d.l.
HNK-1	F	K?	1949	n.a.	194	578	n.a.	n.a.	378	141	1.68	0.18	1.53
TOM-191	F	N.K.	3733	n.a.	18.9	465	n.a.	n.a.	229	64.8	0.19	0.10	0.010
TOM-192	F	N.K.	7669	n.a.	23.8	325	n.a.	n.a.	337	64.4	0.21	0.66	0.011
TOM-193	F	N.K.	1816	n.a.	7.17	242	n.a.	n.a.	440	81.3	0.77	0.24	0.214
TOM-194	F	N.K.	3282	n.a.	778	317	n.a.	n.a.	565	59.4	0.23	0.10	0.035
TOM-195	F	N.K.	3936	n.a.	415	450	n.a.	n.a.	852	86.7	0.45	0.50	0.211
TOP-1	V	P.D.	17223	9.92	167	3833	96.3	130	908	118	2.58	1.35	0.82
TOP-2	V	P.D.	28113	10.5	267	4106	38.5	185	105	22.0	2.41	1.21	0.69
TOP-3	V	P.D.	55724	4.89	394	2249	56.9	139	655	104	1.24	0.62	0.59
TOP-4	V	P.D.	6719	6.70	281	2829	50.2	205	79.8	24.4	1.68	0.57	0.14
TOP-6	V	P.D.	9128	3.06	194	1245	32.7	104	356	113	0.67	0.65	0.14
TOP-7	V	P.D.	9535	14.6	228	6001	41.2	115	357	115	16.4	0.74	0.75
TOP-8	V	P.D.	13497	7.71	191	2981	45.9	239	35	15.9	1.99	0.61	0.18
TOP-9	V	P.D.	15267	29.7	390	11279	73.6	163	236	118	7.19	1.64	0.40

Sample	Type	Date	Mg	V	Mn	Fe	Cu	Zn	Sr	Ba	Nd	Pb	U
TOP-10	V	P.D.	119523	9.49	858	3546	82.8	216	678	49.9	2.53	0.61	0.20
TOP-11	V	P.D.	10677	5.38	155	2118	37.4	198	159	13.6	1.13	0.73	0.37
Dongola													
DET-1	H	L.P.	2445	0.55	86.1	272	0.46	194	209	12.7	0.21	0.16	0.005
SEL-1	H	N.K.	2389	4.28	40.2	241	0.32	158	321	51.9	0.36	0.40	0.012
SEL-2	H	N.K.	4561	0.14	9.97	233	0.21	141	253	8.68	0.02	1.76	0.004
SEL-3	H	N.K.	6892	0.10	3.53	203	0.40	158	167	1.85	0.04	1.75	0.002
SEL-4	H	N.K.	3247	1.24	8.80	296	0.27	239	356	8.23	0.15	0.38	0.013
SEL-5	H	N.K.	4367	0.07	3.72	244	0.31	207	432	10.2	0.02	2.66	0.002
SEL-6	H	N.K.	3871	0.41	19.3	262	0.09	170	507	8.08	0.07	1.12	0.004
SEL-7	H	N.K.	2948	0.95	12.1	245	0.16	241	258	4.34	0.29	0.14	0.022
SEL-8	H	N.K.	3666	3.75	8.45	325	0.04	250	410	14.3	0.33	2.10	0.027
SEL-9	H	N.K.	2770	9.35	14.8	250	0.42	199	464	45.2	0.13	2.71	0.018
SEL-10	H	N.K.	7132	0.38	20.1	376	0.25	287	325	5.86	0.04	6.38	0.018
SEL-11	H	N.K.	3844	0.06	6.85	246	0.01	241	325	4.96	0.02	1.67	b.d.l.
SEL-12	H	N.K.	5103	0.22	13.2	208	0.25	145	188	12.2	0.03	8.85	0.002
SEL-13	H	N.K.	3164	0.47	9.70	199	0.24	151	361	18.3	0.06	0.20	0.003
SEL-14	H	N.K.	4916	0.29	20.5	209	1.48	237	171	3.92	0.08	0.41	0.004
SEB-1	H	N.K.	2972	0.04	2.68	136	0.24	106	204	1.32	0.01	0.40	0.0012
SEB-2	H	N.K.	4611	0.05	2.12	162	0.27	132	244	1.45	0.02	0.39	0.0009
SEB-3	H	N.K.	5430	0.12	4.08	165	0.57	126	187	2.33	0.03	0.40	0.0078
SEB-4	H	N.K.	4848	0.03	4.15	153	0.37	157	229	2.06	0.02	0.17	0.0004
SEB-5	H	N.K.	5495	0.05	2.89	151	0.31	143	102	1.77	0.03	0.46	0.0018
SEB-6	H	N.K.	4785	0.30	22.6	160	0.84	162	277	4.63	0.03	3.24	0.0025
DON-1	V	P.D.	1195	1.44	19.8	659	2.40	6.27	50.3	4.91	0.59	0.22	0.050
DON-2	V	P.D.	1120	2.22	29.1	974	3.54	3.80	26.7	17.2	0.76	0.23	0.060
DON-3	V	P.D.	2118	1.24	52.2	558	1.56	9.16	50.7	6.04	0.47	0.14	0.030
Shendi													
SRA-1	H	Meriotic	3719	3.56	14.8	328	10.2	313	402	13.8	0.20	0.46	0.011
SRA-2	H	Meriotic	2555	2.22	26.1	184	1.08	167	343	12.2	0.34	0.17	0.012
SRA-3	H	Meriotic	2844	2.19	59.8	267	0.79	202	285	38.3	0.71	0.14	0.021
SRA-4	H	Meriotic	3527	1.85	13.9	224	0.43	178	395	15.3	0.28	0.28	0.056
SRA-5	H	Meriotic	2258	2.41	14.7	162	0.30	151	521	84.9	0.18	0.11	0.026
SRA-6	H	Meriotic	3182	0.33	10.3	203	0.88	139	483	12.9	0.06	0.09	0.008
SRA-7	H	Meriotic	2747	3.53	5.60	156	b.d.l.	139	399	9.51	0.11	0.06	0.013
SRA-8	H	Meriotic	4064	0.88	19.9	281	1.86	278	710	14.1	0.12	0.80	0.004
Askut													
ASK-15	F	M.K.	6706	n.a.	12.5	265	n.a.	n.a.	306	75.4	0.05	0.20	b.d.l.
ASK-16	F	M.K.	7893	n.a.	7.34	157	n.a.	n.a.	315	84.6	0.01	0.12	b.d.l.
ASK-17	F	M.K.	8680	n.a.	38.6	217	n.a.	n.a.	291	97.7	0.06	0.09	b.d.l.
ASK-18	F	M.K.	2904	n.a.	120	405	n.a.	n.a.	597	81.5	0.13	0.17	0.02
ASK-19	F	N.K.	6378	n.a.	23.6	253	n.a.	n.a.	445	90.2	0.06	0.14	b.d.l.
ASK-20	F	N.K.	5988	n.a.	5.91	180	n.a.	n.a.	316	108	0.04	0.10	0.04
ASK-21	F	N.K.	4820	n.a.	29.6	193	n.a.	n.a.	380	72.1	0.06	0.08	0.01
ASK-22	F	N.K.	2417	n.a.	4.99	207	n.a.	n.a.	322	11.0	0.04	0.08	b.d.l.
ASK-23	F	N.K.	2631	n.a.	48.2	387	n.a.	n.a.	569	78.8	0.29	0.15	0.03
ASK-24	F	N.K.	2473	n.a.	34.2	316	n.a.	n.a.	392	60.4	0.28	0.13	b.d.l.
ASK-25	F	N.K.	2735	n.a.	12.1	198	n.a.	n.a.	212	18.0	0.04	0.30	b.d.l.
ASK-26	F	N.K.	7031	n.a.	288	190	n.a.	n.a.	852	51.3	0.22	0.99	0.15
ASK-27	F	2nd Int. P.	6389	n.a.	10.9	212	n.a.	n.a.	267	147	0.08	0.12	b.d.l.
ASK-28	F	2nd Int. P.	4741	n.a.	21.5	164	n.a.	n.a.	518	106	0.02	0.34	0.01
ASK-29	F	2nd Int. P.	3325	n.a.	9.91	237	n.a.	n.a.	286	91.8	0.06	0.19	0.04
ASK-30	F	M.K.	14659	n.a.	689	42689	n.a.	n.a.	359	463	19.3	9.43	0.90
Abri													
ABR-1	V	P.D.	11032	3.86	282	1544	17.0	117	164	36.6	1.01	0.75	0.09
ABR-2	V	P.D.	33429	7.37	297	3176	14.7	100	1005	146	2.29	2.68	0.23
ABR-3	V	P.D.	14822	18.7	232	7233	13.8	218	1565	283	4.78	5.75	0.71
ABR-4	S	P.D.	1364	26.2	86.1	6741	6.41	17.1	38.6	102	6.00	4.27	0.43
Wadi Halfa													
WH-1	V	P.D.	10735	12.6	210	5142	27.7	193	734	68.4	4.34	4.93	0.37
WH-3	V	P.D.	38709	11.1	423	4381	67.3	333	1039	119	3.49	7.40	1.11
WH-4	V	P.D.	10311	16.2	392	5973	81.6	365	204	49.1	5.38	4.53	0.44
WH-5	V	P.D.	9305	8.08	492	3666	60.2	369	228	243	2.11	0.96	0.21
WH-6	V	P.D.	10140	8.10	619	3212	53.9	267	202	62.3	2.56	2.30	0.23
WH-7	V	P.D.	21003	4.14	796	1794	15.6	60.3	72.8	10.5	1.24	1.73	0.09
WH-8	V	P.D.	16315	15.5	436	6131	45.2	116	1200	407	5.35	5.41	0.26
WH-9	V	P.D.	8807	2.08	1259	1035	26.3	128	343	225	0.61	0.83	0.07
WH-10	V	P.D.	23502	16.5	371	6207	25.2	154	1882	185	5.56	6.52	0.37
WH-11	S	P.D.	1737	64.6	523	26745	30.9	136	100	161	24.9	8.10	1.7

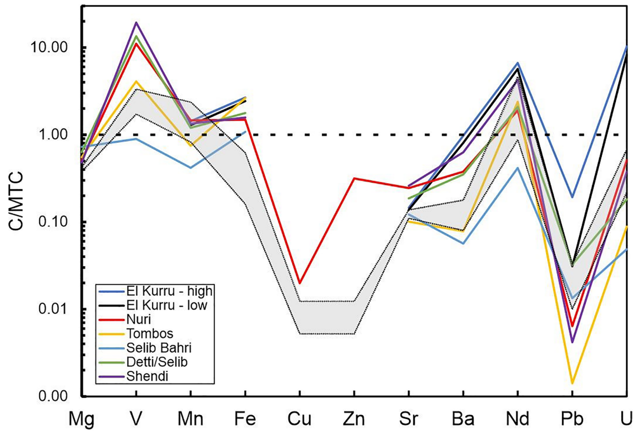

Figure 2. Log plot illustrating average concentrations (C) of trace elements for tooth enamel investigated here from various burial sites divided by Mean Threshold Concentration (MTC) values for each element from Kamenov et al. (2018). Elements with C/MTC values > 1.0 (dashed line) are interpreted to have been affected (increased) by postmortem alteration. Field outlined in gray represents range of trace element concentrations (average values plus 1 sigma standard deviation) for typical, non-altered fossilized tooth enamel sample (from Kamenov et al. 2018).

Analytical Methods

Trace element geochemistry

Mechanically cleaned and cut enamel samples were digested and processed at the University of Notre Dame Midwest Isotope and Trace Element Research Analytical Center (MITERAC) using established methodologies summarized below. Samples of tooth enamel were processed in two steps. In the first step, between ~70 and ~300 mg of enamel was placed in a 15 mL Savillex® Teflon beaker and ~4 ml of concentrated 16N, ultrapure HNO_3 was added; this mixture was then heated on a hotplate at 110° C for 24 hours. After the heating, samples were removed from the hotplate and cooled for one hour. After rinsing the sample residues adhered to the sides of the beakers with ultrapure water (18 MΩ cm^{-2}), samples were placed back on the hotplate to achieve complete dryness. In the second cycle, all conditions were kept the same, except the amount of ultrapure 16N HNO_3 acid was decreased from 4 to 1 mL. After the last drying step, 5 mL of ultrapure 16N HNO_3 acid was added into the beaker and the solution diluted with ultrapure water until a final total volume of ~25 mL was achieved. For botanicals, digestion and preparation of samples was identical to that for enamel, with the exception that ~1 ml aliquots of ultrapure concentrated (~10 M) H_2O_2 acid were periodically added to the 16N HNO_3 while samples were on the hotplate to oxidize and to eliminate the organic content. Sample volume aliquots for trace element and Sr, Nd and Pb isotope analyses were taken from the 25 mL solution.

The trace element abundances (Table 2) for all samples were determined using an Attom (Nu Instruments Ltd., Wales, UK) high-resolution, inductively coupled plasma mass spectrometer (HR-ICP-MS) in medium mass resolution mode ($M/\triangle M \approx 3000$). Samples were processed using a wet plasma solution mode introduction system that consists of a cyclonic spray chamber (housed within a Peltier cooling device at 7 °C) and Meinhard nebulizer (aspiration rate of 0.1 mL/min). Before each analytical session, the Attom instrument was tuned and calibrated using a multi-elemental (Li, B, Na, Si, Sc, Co, Ga, Y, Rh, In, Ba, Lu, Tl, U) 1 ppb (ng g-1) standard solution. The concentrations of the trace elements (Table 2) were determined by an external calibration method, which includes correction for matrix effects and instrumental drift. The multi-element standard solution used for the calibration curve consists of a mixture of high purity, certified (abundances) commercial single element solutions. Given the use of ultrapure reagents and sample processing in class 1000 cleanroom laboratories, blank levels for all trace elements investigated here were monitored and are at the 10 to 100s of picograms level, and are therefore insignificant (several magnitude levels lower) compared to the total amount of analyte processed for each element.

Sr isotope compositions

Separation and purification of Sr for subsequent Sr isotope analysis involved ion exchange chromatography, which employed columns containing 4.3 mL of 200-400 mesh AG50W-X8 resin. Sample aliquots (containing ~300 ng total Sr) in 1 mL of ultrapure 2.5N HCl were loaded onto the resin beds; this was followed by several additional wash steps of ultrapure 2.5N HCl acid, and the Sr was subsequently eluted with 10 mL of ultrapure 2.5N HCl. After the ion exchange chemistry, Sr-bearing aliquots were dried, dissolved in 2% HNO_3 solution (~2 mL) and aspirated into the ICP torch using a desolvating nebulizing system (DSN-100 from Nu Instruments Ltd.). Strontium isotope measurements were conducted using a NuPlasma II MC-ICP-MS (multi-collector inductively coupled plasma mass spectrometer; Nu Instruments Ltd.) instrument according to the protocol outlined in Balboni and colleagues (2016). Strontium isotope data were acquired in static, multi-collection mode using five Faraday collectors for a total of 400 s, consisting of 40 scans of 10 s integrations. The analytical protocol's accuracy and reproducibility were verified by analyzing the NIST SRM 987 strontium isotope standard during two analytical sessions, which yielded an average value of 0.710230 ± 0.000040 (2σ; n = 32), in agreement with the certified value of 0.71025 (Faure and Mensing 2005).

Neodymium isotope compositions

For purification of neodymium (Nd), the rare earth elements (REEs) were first separated during the Sr ion exchange chemistry. Subsequently, Nd was isolated from the remaining REEs on 9.7 cm columns containing 1.22 mL 50–100 mesh Eichrom Ln-Spec resin. The resin was cleaned with ultrapure 6N HCl and conditioned with 0.18N HCl while Nd was collected with 0.3N HCl. Purified Nd aliquots were dried down and brought back into ~2 mL of 2% HNO_3 for analysis. Neodymium isotope data were acquired in static, multi-collector mode using seven Faraday collectors. Instrumental mass bias was corrected for using the $^{146}Nd/^{144}Nd$ ratio (0.7219) while accuracy and reproducibility were assessed via repeated measurements of the JNd_i-1 standard, which yielded an average $^{143}Nd/^{144}Nd$ of 0.512090 ± 0.000016 (2σ; n = 19), in good agreement with the accepted value (0.512115; Tanaka et al. 2000).

Lead isotope compositions

The lead (Pb) separation method is adapted from Manhes et al. (1980) and a brief summary is provided here (after Koeman et al. 2015). The Pb ion-exchange microcolumns consist of approximately 20 μL of clean AG1-X8 resin (75–150 mesh) placed into a polypropylene tube combined with a polystyrene frit. The resin volume is cleaned using 5 mL each of ultrapure water and 6N HCl, and further conditioned with 0.15 mL of ultrapure 0.8 N HBr. The sample solution was loaded with 0.6 mL of 0.8 N HBr, washed twice with 0.15 mL of 0.8 N HBr, and finally eluted with 0.7 mL of 6 N HCl acid. After the eluted Pb is dried down, the ion-exchange procedure is repeated with fresh resin in order to further purify the Pb aliquot. Following the last elution procedure, the Pb aliquot is dried down and dissolved in 2% HNO_3 for solution mode MC-ICP-MS analysis.

Pb isotope compositions of the sample solutions were determined using the same procedure outlined in Simonetti and colleagues (2004). After the purification steps, the aliquot of Pb was spiked with a NIST SRM 997 Thallium standard solution (2.5 ppb). Seven Faraday cups on the Nu Plasma II MC-ICPMS instrument were employed to simultaneously measure the Pb and Tl isotopes and ^{202}Hg. The instrumental mass bias (exponential law; $^{205}Tl/^{203}Tl = 2.3887$) is determined by measuring the $^{205}Tl/^{203}Tl$, and ^{202}Hg is monitored to correct for the interference of ^{204}Hg on ^{204}Pb. Prior to the aspiration of the samples into the plasma, ion signals for the gas and acid blanks ("on-peak-zeros") were recorded for 30 s to determine baseline values. For each analysis, data acquisition involved two blocks of 25 scans (each scan has a 10 s integration time). A 25-ppb solution of the NIST SRM 981 Pb standard (spiked with 6 ppb NIST SRM 997 Tl standard) was measured periodically during the analytical session in order to validate the Pb isotope results. The average Pb isotope ratios and associated 2σ standard deviations obtained on 27 measurements of the NIST SRM 981 Pb isotope standard for the pertinent analytical sessions are as follows: $^{206}Pb/^{204}Pb = 16.937 \pm 0.004$, $^{207}Pb/^{204}Pb = 15.493 \pm 0.003$, $^{208}Pb/^{204}Pb = 36.703 \pm 0.009$, $^{208}Pb/^{206}Pb = 2.16705 \pm 0.00070$, and $^{207}Pb/^{206}Pb = 0.91472 \pm 0.00021$, which overlap with the certified values for this standard (Baker et al. 2004).

Results

Trace elements and radiogenic Sr, Nd, and Pb isotope compositions

In relation to the Sr isotope compositions of the enamel samples studied here, as reported in previous investigations (Buzon et al. 2007; Simonetti et al. 2021), the abundances of Sr for the majority of samples define a range of values from ~100 to ~500 ppm (Table 2); these yield C/MTC values that are < 1 (Fig. 2) and are not correlated with their corresponding $^{87}Sr/^{86}Sr$ compositions (not shown). Given the significant number of Sr and Nd isotope compositions being reported here for various types of samples (enamel, faunal, botanical, soil), the data have been subdivided and are illustrated based on geographic location. The data are divided into two main geographic groups; one consists of samples from the southern part of the NRVS, proximal to the Fifth Cataract and include samples from El-Kurru, Nuri and Shendi burial sites (Fig. 3); the second group consists of samples from the middle region of the NRVS between the Wadi Halfa and Dongola regions (Fig. 4).

Figure 3 displays the present-day Sr and Nd isotope compositions (equivalent ε_{Nd} values; defined in figure caption) for various samples examined here from the southern region of the NRVS on a typical Nd-Sr isotope diagram. The Sr and Nd isotope compositions all plot within the enriched quadrant of the diagram (Fig. 3), and the salient results are as follows: (1) The two main enamel groups from El-Kurru (as defined by Simonetti et al. 2021) are characterized by similar ε_{Nd} values (range from ~−2 to 0), and these mainly overlap the range of Sr-Nd isotope compositions for faunal samples from nearby Nuri; (2) the Sr-Nd isotope composition for modern-day soil from Nuri is less radiogenic (i.e., higher Sr isotope ratios and lower ε_{Nd} values) compared to the older faunal samples for the same site; (3) the Sr-Nd isotope ratios for botanical

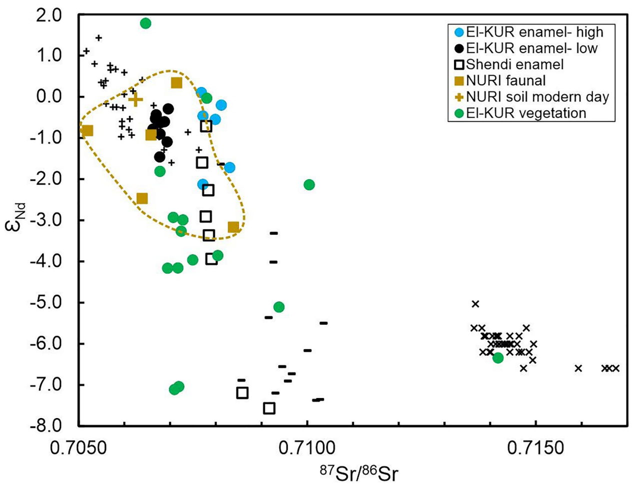

Figure 3. Diagram plots $^{87}Sr/^{86}Sr$ compositions against their corresponding ε_{Nd} values for various sample types investigated here from burial sites within the southern region of the NRVS. ε_{Nd} values are calculated by taking present-day $^{143}Nd/^{144}Nd$ ratios for samples studied here (Table 3) and divided by the present-day chondritic uniform reservoir (CHUR) = 0.512638 (Faure and Mensing, 2005), then subtracting by one and then multiplying by 10,000. For comparative purposes, also plotted are: (X) = Samples of North African dust (Jung et al. 2004); (–) = Red Sea Hills wadi mud (Fielding 2015); (+) = Holocene mud floodplain deposits in the Northern Dongola Reach (Woodward et al. 2015).

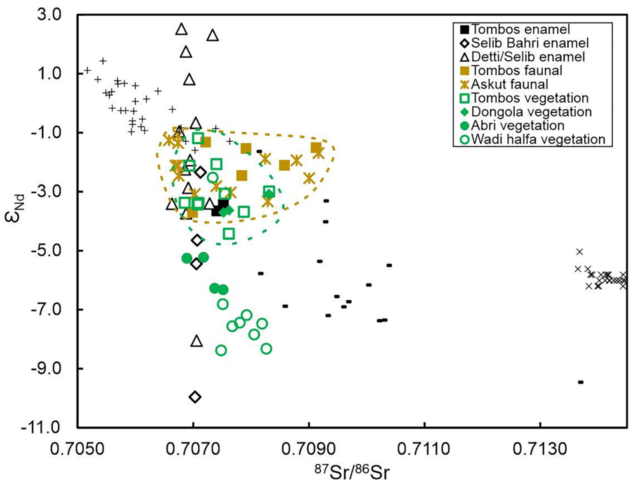

Figure 4. Diagram illustrates $^{87}Sr/^{86}Sr$ compositions against their corresponding ε_{Nd} values for various sample types investigated here from burial sites within the Tombos-Dongola regions of the NRVS. Dashed brown line outlines overlapping range of Nd-Sr isotope compositions for faunal samples from both Tombos and Askut regions. Green dashed line delineates Nd-Sr compositions of present-day botanical samples from Tombos. For comparative purposes, also plotted are: (X) = Samples of North African dust (Jung et al. 2004); (–) = Red Sea Hills wadi mud (Fielding 2015); (+) = Holocene mud floodplain deposits in the Northern Dongola Reach (Woodward et al. 2015).

samples from El-Kurru are highly variable but are mainly more radiogenic compared to the enamel samples from El-Kurru; and (4) most of the enamel samples from the Shendi region define a vertical array in that they are characterized by relatively uniform Sr isotope ratios and variable ε_{Nd} values.

The Nd-Sr isotope diagram for samples from the middle NRVS is shown in Figure 4, which illustrates the following important results: (1) A majority of the faunal samples from Askut and Tombos and plants from the Dongola region indicate fairly consistent ε_{Nd} values (range from ~–1 to ~–3) and variable Sr isotope compositions; (2) the two enamel samples from Tombos overlap the Sr-Nd isotope field for the faunal samples from this region; and (3) the enamel samples from the Dongola region (Selib Bahri and Detti/Selib) define vertical arrays that show significant overlap with Sr-Nd isotope compositions for faunal and modern-day botanical samples from Tombos; moreover, the latter show complete overlap with the Sr-Nd isotope compositions for faunal samples from Tombos (Fig. 4), indicating that the Sr-Nd isotope composition of the Tombos region has not changed over the last ~5000 years; and (4) in contrast, the samples of modern-day plants from both the Abri and Wadi Halfa regions are shifted to distinctly more radiogenic Sr-Nd isotope compositions compared to proximal faunal/matrix samples at Askut. Importantly, the Sr, Nd, and Pb isotope data for the botanical samples investigated here do not correlate with the depth of their root system.

For comparative purposes, the Sr-Nd isotope diagrams (Figs. 3 and 4) contain the fields outlined by the Nd and Sr isotope compositions for Holocene alluvial deposits in the Northern Dongola Reach (Woodward et al. 2015), North African dust (Jung et al. 2004) and Red Sea Hills wadi mud (Fielding 2015). Woodward and colleagues (2015) argued that the Nd-Sr isotope systematics of the Nile River mud deposits (+) were likely the result of bulk mixing involving three components: North African dust (×), wadi mud from the Red Sea Hills (–), and the primitive, mantle-like isotope signatures derived from Ethiopian basalts (not shown; Kieffer et al. 2004; Pik et al. 1999, 2008). There is minimal overlap between the Nd-Sr isotope signatures for enamel samples investigated here and those recorded in the Nile River mud deposits and Red Sea Hills region. Of note, the Nd-Sr isotope characteristics of botanical samples from Abri and Wadi Halfa regions plot outside the mixing curves outlined by Woodward and colleagues (2015; Fig. 4), and therefore necessitate the presence of an additional crustal component within the NRVS.

Lastly, in the Pb-Pb isotope diagrams (Figs. 5 and 6), the Pb isotope data reported here are compared to Pb isotope compositions obtained for surface sediments within the Bodélé Depression in southeastern Chad within the central Sahara/Sahel region of Northern Africa (Abouchami et al. 2013); the latter is considered one of the largest sources of mineral dust on Earth (Prospero et al. 2002). As can be clearly seen in

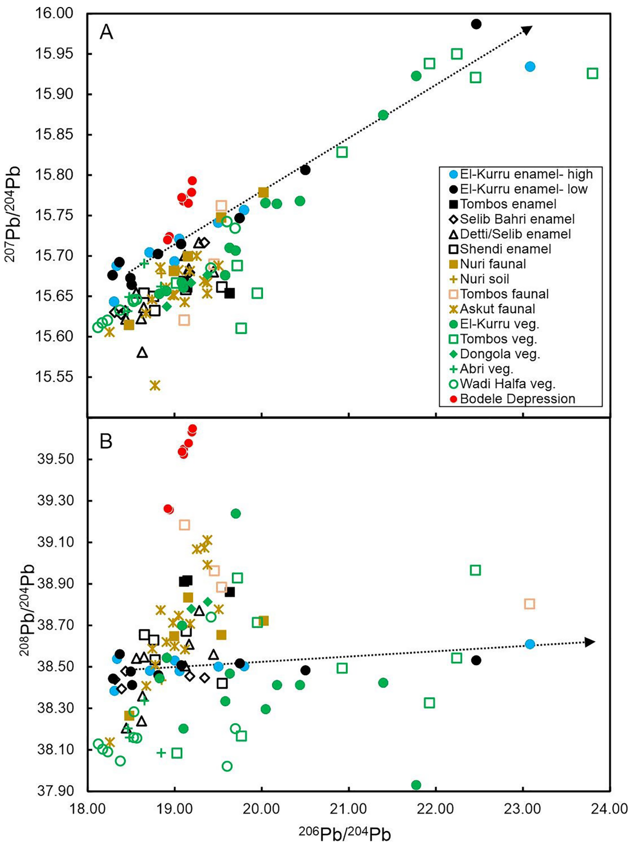

Figure 5. $^{207}Pb/^{204}Pb$ vs. $^{206}Pb/^{204}Pb$ (A) and $^{208}Pb/^{204}Pb$ vs. $^{206}Pb/^{204}Pb$ (B) isotope plots illustrating Pb isotope ratios for enamel, faunal, and present-day botanical samples investigated here from the different regions of the NRVS. Shown for comparison are the Pb isotope compositions for dust samples from the Bodélé Depression, Sahara Desert (Abouchami et al. 2013). The dashed line with arrow defines the groundwater-controlled, postmortem alteration trend based on enamel samples from El-Kurru (as defined by Simonetti et al. 2021). Uncertainties (2σ level) associated with individual $^{208}Pb/^{207}Pb$ and $^{207}Pb/^{206}Pb$ ratios are within the size of the symbol.

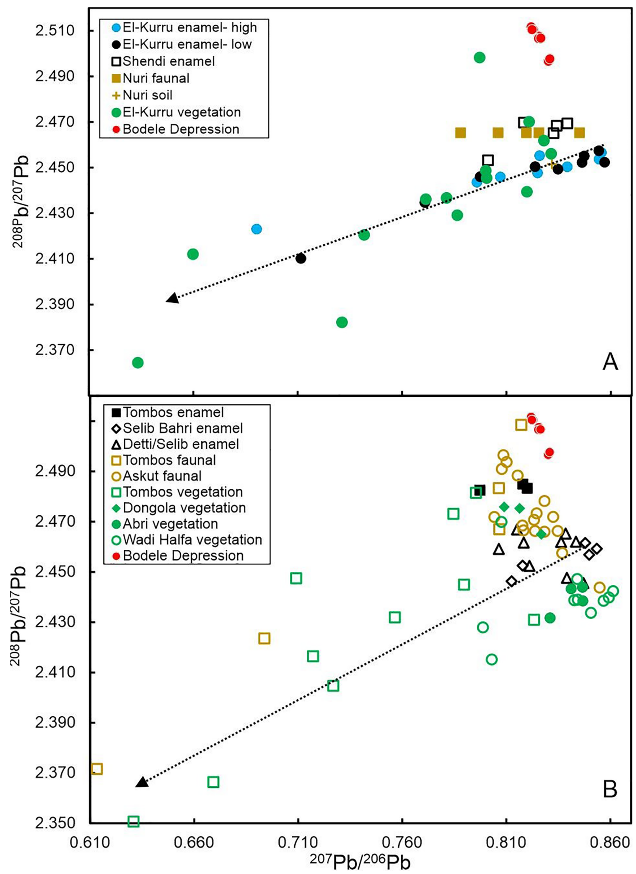

Figure 6. $^{208}Pb/^{207}Pb$ vs. $^{207}Pb/^{206}Pb$ isotope plots illustrating Pb isotope ratios for enamel, faunal, and present-day botanical samples investigated here from the southern regions (A) and Tombos-Dongola (B) regions of the NRVS. Shown for comparison are the Pb isotope compositions for dust samples from the Bodélé Depression, Sahara Desert (Abouchami et al. 2013). The dashed line with arrow defines the groundwater-controlled, post-mortem alteration trend based on enamel samples from El-Kurru (as defined by Simonetti et al. 2021). Uncertainties (2σ level) associated with individual $^{208}Pb/^{207}Pb$ and $^{207}Pb/^{206}Pb$ ratios are within the size of the symbol.

Figures 5 and 6, there is essentially no overlap between the Pb isotope compositions for the surface sediments from the Bodélé Depression and those for all enamel samples investigated here.

Discussion

Evaluation of the climate change impact hypothesis

Typical Saharan dust is composed primarily of sand (quartz; ~60 to 80 wt% SiO_2; e.g., Abouchami et al. 2013; Chester et al. 1972; Middleton and Goudie 2001), and quartz does not contain a significant amount of trace element impurities due to its compact crystalline (framework tetrahedral) structure. Moreover, Sr abundances (~25 to 66 ppm) are particularly low in Saharan dust due to high solubility and removal of Sr (and Ca) from the surface during weathering prior to sediments becoming airborne (Abouchami et al. 2013). Therefore, the low Sr abundances of aeolian dust make it very difficult (mass balance perspective) to change the Sr isotope composition of the local bioavailable Sr. Furthermore, incorporation of silicate-hosted Sr from aeolian sources into the human body requires for it to be exchanged and mixed with blood Sr (buffered by bone Sr), and fixed into body tissues including tooth enamel, along with contributions from other food stuff (Weber et al. 2020). For example, Bataille and colleagues (2018) have indicated that clay modal contents in soil may have a strong impact on the local bioavailable Sr isotope composition. Similarly, in laboratory-controlled experiments, Weber and colleagues (2020) showed that enamel of rodents fed kaolinite-enriched pellets did record a shift towards higher, more radiogenic Sr isotope compositions. Additionally, tooth wear, also known as attrition, which was cited by Woodward and colleagues (2015) as evidence for the increasing contribution of aeolian dust within the NRV, could be attributed to grit emanating from grinding stones. The typical Nile Valley diet included bread and beer (Samuel 1993) processed from stone quern and mortar implements (Ruffer 1920); as a result, grain contained grit from the grinding stone, which accelerated dental attrition (Zakrzewski et al. 2016). The grinding vessels used were made of quartz and, as stated above, since quartz contains negligible strontium, its ingestion would not alter an individual's strontium isotopic composition.

The process of incorporating radiogenic, aeolian-based strontium into plants, which is then transferred into bioavailable strontium for humans is not a rapid process since it takes tens of thousands of years for trees and plants to acquire the Sr isotope signature of aeolian dust (e.g., Coble et al. 2015). Also, the Sr isotopic fingerprint of aeolian dust becomes a significant factor only when carbonate sources are being weathered (van der Hoven and Quade 2002). Since aeolian dust within the NRVS consists mainly of weathered silicate material, the amount of bioavailable Sr for humans and plants is limited. Assuming there was a climatic shift to more arid conditions over the past ~1,500 years, the change in bioavailable Ca (and Sr) for humans and plants (if present) would not be instantaneous. Moreover, based on the van der Hoven and Quade (2002) investigation, the resultant Sr isotope composition of bioavailable Sr in the NRVS will reflect a mixing of two components that may be assessed by mass balance calculations. It would not consist solely of a more distal aeolian source completely masking the pedogenic Sr from local sources.

A hypothesis that a drying climate has impacted the isotope signatures of bioavailable Sr in the NRVS must consequently result in increasing (higher) strontium isotope values through time. The Sr isotope signature for a particular time period may then be established using both faunal (foraging animal, soil matrix) and human samples. The archaeological human and contemporary archaeological faunal material originating from the same location for a given time period should record similar or identical Sr, Nd, and Pb isotope signatures since both animals and humans have been exposed to similar environmental conditions.

Implications of new radiogenic (Sr, Nd, and Pb) isotope data

Although the remaining samples of enamel for each burial site investigated here define a certain degree of variability with regard to their ε_{Nd} values, their corresponding Sr isotope values are nonetheless relatively consistent. For example, samples from the Shendi region (with the exception of SRA-2 and -3 as explained above), yield variable ε_{Nd} values that range between −0.7 and −4.0, but are characterized by similar Sr compositions (vary between 0.7077 and 0.7079) such that they define vertical arrays in both the Nd-Sr isotope diagrams (Figs. 3 and 4); similar vertical arrays are also defined by enamel samples from the El-Kurru and Dongola region burial sites investigated here (Figs. 3 and 4). These features indicate that their $^{87}Sr/^{86}Sr$ ratios have remained buffered against any possible postmortem alteration due to the relatively high concentrations of Sr (> 100 ppm; Table 2). Interpretation of the variable ε_{Nd} values for enamel samples analyzed here is complex and beyond the scope of this investigation, in particular due to the factors cited earlier and summarized in Plomp and colleagues (2019), which include: (1) lack of bioavailable Nd in food (ppb range; Goldstein and Jacobsen 1987; Kulaksiz and Bau 2013; Tyler 2004), (2) absence of physiological or biological function of Nd in the human body (Evans 1990), and (3) incompatible substitution of trivalent ion (Nd^{3+}) for calcium (Ca^{2+}) in the hydroxyapatite crystal lattice of human bone and teeth (Evans 1990; Plomp et al. 2017). Obviously, these factors do not apply to the ε_{Nd} values for faunal, soil, and botanical samples investigated here, and therefore can be used to monitor possible temporal shifts in the bioavailable Sr, Nd and Pb isotope compositions within the NVRS.

If there is indeed a diachronic shift recorded in the Sr isotope compositions for tooth enamel samples from within the NRVS during the past ~7,000 years resulting from an increased amount of wind-derived dust from the neighboring Sahara, the Sr and Pb isotope ratios should increase and ε_{Nd} values decrease as time approached present day. For example, aeolian dust from the Sahara is characterized by high $^{87}Sr/^{86}Sr$ ratios (> 0.7140) and low ε_{Nd} values (< −5.0 to −13.0, Figs. 3 and 4; Abouchami et al. 2013; Jung et al. 2004). Ultimately, the isotopic compositions should verge toward the signatures for present-day plants, based on the assumption that the latter is sampling an increasing amount of bioavailable Sr with a greater component of Saharan aeolian dust.

The new Sr, Nd and Pb isotope data reported in this study define several intriguing features. First, all samples, faunal, enamel, and present-day plants from the Tombos burial site are characterized by similar and overlapping Sr and Nd isotope compositions (Fig. 4). This result suggests that the Sr-Nd isotope composition of the natural environment within the Tombos region has remained static for the past ~3,500 years, which is obviously not consistent with the aeolian dust impact hypothesis. Second, as stated earlier, it is generally assumed that the contribution of bioavailable atmospheric Sr gradually decreases with soil depth (Capo et al. 1998; Vitousek et al. 1999). However, the Sr, Nd, and Pb isotope data for the botanical samples investigated here (Table 2) do not correlate with regard to the depth of their root system within a given burial site or the NRVS as a whole; this feature also corroborates the lack of significant contribution of atmospheric Sr to the NRVS during the Holocene Epoch. Third, the present-day sample of soil from the Nuri burial site is less radiogenic (i.e., characterized by a lower Sr isotope ratio and higher ε_{Nd} value) than the older faunal samples from the same site (Fig. 3). This contrasts with what would be expected if aeolian dust from the Sahara has been accumulating over the past ~3,500 years in the NRVS, which is characterized by much higher $^{87}Sr/^{86}Sr$ ratios (> 0.7140 to ~0.7293, Figs. 3 and 4; Abouchami et al. 2013; Guinoiseau et al. 2022; Jewel et al. 2021; Jung et al., 2004) than the geological background within the NRVS.

An alternative explanation is that the radiogenic contribution from aeolian Saharan dust has yet to become a major component of the bioavailable Sr within the NRVS; in other words, the process of elemental bioavailability may take more than the ~7,000 years of archaeological record covered in this study. Also of importance, Saharan-Sahelian dusts are blown to the west by the prevailing easterlies (opposite direction to NRVS), across the tropical Atlantic Ocean toward North America, the Caribbean, and South America, depending on the seasonal position of the Inter-Tropical Convergence Zone (ITCZ; Guinoiseau et al. 2022 and references therein). Hence, given this combined evidence, it is clear that the Saharan aeolian component has not contributed in any significant manner to the bioavailable Sr record for the burial sites within the NRVS examined here. As stated earlier, soil development and renewal in relation to its budget of bioavailable Sr is influenced by several contributions, which include not only atmospheric sources of Sr but also water (e.g., Nile River) and the local geologic background.

Figure 7 illustrates literature Sr isotope compositions compiled from published samples of enamel, a variety of faunal, and present-day sediments/soil within the NRVS, along with the new isotope data obtained here (Table 3) that are plotted against their corresponding reported ages; the latter range between ~7,000 years before present to present-day. If the aeolian dust hypothesis (Woodward et al. 2015) is indeed valid, then it can be assumed that the $^{87}Sr/^{86}Sr$ signatures of archaeological samples should increase with decreasing age. However, this is clearly not the case for the Sr isotope data displayed in Figure 7. In general,

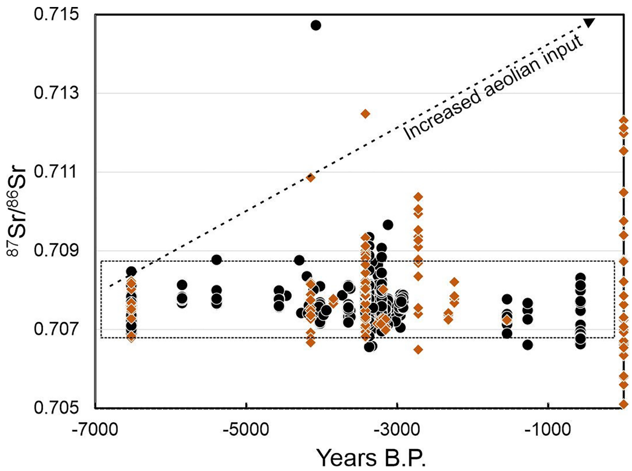

Figure 7. Time (years before present) versus $^{87}Sr/^{86}Sr$ ratios for samples investigated here (Table 3) and those from literature data for samples located within the NVRS. Filled black circles = human enamel samples; Filled brown (gray) diamonds = faunal samples. Published literature data are taken from the following previous investigations: Buzon and colleagues (2007); Buzon and Simonetti (2013); Dominy and colleagues (2020); Gregoricka and Baker (2021); Herrick (2018); Kozieradzka-Ogunmakin (2021); Maritan and colleagues (2021); Osypinska and colleagues (2021); Retzmann and colleagues (2019); Schrader and colleagues (2019); Simonetti and colleagues (2021); Stantis and colleagues (2020); Stantis and colleagues (2021); Touzeau and colleagues (2013). For the purposes of clarity, the age adopted for a suite of samples from an individual burial site shown here is illustrated as the midpoint of the age range reported for the time period.

$^{87}Sr/^{86}Sr$ ratios for tooth enamel samples have remained constant during the last ~7,000 years, and for each group of samples of similar age, the Sr isotope signatures for tooth enamel overlap with those for their corresponding faunal samples. Of particular interest, the Sr isotope compositions for samples of present-day plants also overlap with those for older enamel and faunal samples. Thus, if there has been an increase in wind-derived material originating from the neighboring Sahara, then this has not impacted the budget of bioavailable Sr incorporated within tooth enamel and faunal samples from the NRVS during the past ~7,000 years. As stated earlier, possible explanations for the lack of impact may be attributed to a longer residence time for aeolian silicate-hosted Sr to complete the biogeochemical cycle from the atmosphere to soil to finally being metabolized within living organisms (Cobble et al. 2015; van der Hoven and Quade 2002). Moreover, aeolian dust is characterized by much lower Sr contents (Abouchami et al. 2013) compared to that found in the local geological background, which buffers the $^{87}Sr/^{86}Sr$ ratios for the latter against input or contamination from aeolian sources. Also of importance, data for enamel and faunal samples for each time period shown in Figure 7 indicate that the degree of Sr isotope variability has essentially remained constant during the past ~7000 years. Once again, increased contribution from aeolian sources would

Table 3. Sr, Nd, and Pb isotope compositions for samples investigated in this study.

Sample	$^{87}Sr/^{86}Sr$	+/– (1s)	$^{143}Nd/^{144}Nd$	+/– (1s)	ε_{Nd}	$^{206}Pb/^{204}Pb$	+/– (1s)	$^{207}Pb/^{204}Pb$	+/– (1s)	$^{208}Pb/^{204}Pb$	+/– (1s)	$^{208}Pb/^{207}Pb$	$^{207}Pb/^{206}Pb$
El-Kurru													
KUR-1	0.707476	0.000005	0.51261	0.00001	−0.57	23.0812	0.0107	15.9343	0.0009	38.6091	0.0018	2.423	0.690
KUR-2	0.707718	0.000008	0.51253	0.00001	−2.13	19.5028	0.0007	15.7412	0.0003	38.5008	0.0008	2.446	0.807
KUR-3	0.707991	0.000007	0.51261	0.00001	−0.55	18.3083	0.0003	15.6433	0.0003	38.3838	0.0009	2.454	0.854
KUR-4	0.706935	0.000004	0.51258	0.00001	−1.10	56.3512	4.9200	18.0596	0.4330	37.9169	0.2550	2.100	0.318
KUR-5	0.707121	0.000006	n.a.			19.7986	0.0007	15.7567	0.0004	38.5027	0.0007	2.444	0.796
KUR-6	0.706682	0.000009	0.51261	0.00001	−0.53	18.4959	0.0005	15.6725	0.0002	38.4772	0.0007	2.455	0.847
KUR-7	0.708306	0.000008	0.51255	0.00001	−1.72	19.0559	0.0017	15.7209	0.0002	38.4791	0.0007	2.448	0.825
KUR-8	0.708120	0.000008	0.51263	0.00001	−0.20	19.0009	0.0005	15.6931	0.0004	38.5302	0.0010	2.455	0.826
KUR-9	0.706698	0.000007	0.51262	0.00001	−0.44	19.7477	0.0010	15.7468	0.0005	38.5164	0.0011	2.446	0.797
KUR-10	0.706962	0.000005	0.51262	0.00001	−0.30	20.5030	0.0003	15.8063	0.0003	38.4829	0.0007	2.435	0.771
KUR-11	0.707684	0.000007	0.51264	0.00001	0.10	18.7151	0.0003	15.7043	0.0003	38.4809	0.0011	2.450	0.839
KUR-12	0.707720	0.000006	0.51261	0.00001	−0.47	18.3382	0.0002	15.6877	0.0002	38.5385	0.0006	2.457	0.855
KUR-13	0.706877	0.000004	0.51261	0.00001	−0.61	18.8118	0.0002	15.7023	0.0002	38.4596	0.0005	2.449	0.835
KUR-14	0.706783	0.000004	0.51261	0.00001	−0.60	19.0768	0.0004	15.7147	0.0003	38.5075	0.0009	2.450	0.824
KUR-15	0.706627	0.000003	0.51260	0.00001	−0.79	22.4638	0.0076	15.9869	0.0007	38.5312	0.0014	2.410	0.712
KUR-16	0.706782	0.000004	0.51259	0.00001	−0.91	18.3687	0.0003	15.6921	0.0003	38.5612	0.0008	2.457	0.854
KUR-17	0.706787	0.000005	0.51261	0.00001	−0.63	18.5107	0.0004	15.6642	0.0003	38.4121	0.0009	2.452	0.846
KUR-18	0.706774	0.000003	0.51256	0.00001	−1.46	18.2916	0.0004	15.6761	0.0003	38.4431	0.0009	2.452	0.857
KUP-1	0.706947	0.000007	0.51242	0.00001	−4.16	28.0810	0.0010	16.4562	0.0005	38.4077	0.0010	2.334	0.633
KUP-2	0.707190	0.000004	0.51228	0.00001	−7.04	25.6611	0.0012	16.2561	0.0006	38.4363	0.0014	2.364	0.800
KUP-3	0.707497	0.000006	0.51243	0.00006	−3.96	19.6328	0.0005	15.7099	0.0004	38.4674	0.0008	2.449	0.831
KUP-4	0.708044	0.000009	0.51244	0.00001	−3.86	18.8259	0.0003	15.6530	0.0003	38.4445	0.0008	2.456	0.771
KUP-5	0.706467	0.000008	0.51273	0.00001	1.78	20.4398	0.0010	15.7679	0.0007	38.4120	0.0018	2.436	0.797
KUP-6	0.714175	0.000008	0.51231	0.00001	−6.34	19.7014	0.0006	15.7066	0.0004	39.2386	0.0010	2.498	0.660
KUP-7	0.709385	0.000007	0.51238	0.00001	−5.11	24.3135	0.0003	16.0452	0.0002	38.7007	0.0005	2.412	0.801
KUP-8	0.707171	0.000005	0.51242	0.00001	−4.16	19.5820	0.0004	15.6759	0.0003	38.3339	0.0008	2.445	0.828
KUP-9	0.707242	0.000007	0.51247	0.00003	−3.27	18.9086	0.0005	15.6565	0.0005	38.5434	0.0012	2.462	0.821
KUP-10	0.707099	0.000006	0.51227	0.00001	−7.11	19.0850	0.0005	15.6671	0.0004	38.6983	0.0011	2.470	0.731
KUP-11	0.707280	0.000004	0.51248	0.00001	−2.99	21.7744	0.0005	15.9227	0.0004	37.9303	0.0009	2.382	0.820
KUP-12	0.707071	0.000012	0.51249	0.00001	−2.93	19.1014	0.0004	15.6608	0.0003	38.2020	0.0007	2.439	0.742
KUP-13	0.706779	0.000023	0.51255	0.00001	−1.81	21.3956	0.0011	15.8742	0.0004	38.4230	0.0011	2.420	0.781
KUP-14	0.707804	0.000007	0.51264	0.00001	−0.04	20.1755	0.0008	15.7645	0.0006	38.4123	0.0014	2.437	0.786
KUP-15	0.710045	0.000004	0.51253	0.00001	−2.14	20.0452	0.0007	15.7655	0.0005	38.2956	0.0013	2.429	0.633
Nuri													
NUF-1	0.706390	0.000003	0.51251	0.00002	−2.47	20.0216	0.0009	15.7785	0.0008	38.7221	0.0024	2.465	0.788
NUF-2	0.708388	0.000005	0.51248	0.00001	−3.17	19.5366	0.0009	15.7474	0.0007	38.6535	0.0018	2.465	0.806
NUF-3	0.705197	0.000006	0.51260	0.00001	−0.82	19.1544	0.0022	15.6994	0.0021	38.8338	0.0049	2.465	0.820
NUF-4	0.706585	0.000006	0.51259	0.00001	−0.93	18.9943	0.0008	15.6813	0.0007	38.6477	0.0016	2.465	0.826
NUF-5	0.707146	0.000004	0.51266	0.00001	0.34	18.4788	0.0008	15.6145	0.0006	38.2642	0.0017	2.465	0.845
NSO-1	0.706247	0.000003	0.51263	0.00001	−0.06	18.8504	0.0015	15.6784	0.0012	38.4354	0.0030	2.451	0.832
Tombos & Hannek													
TOM-196	0.707468	0.000003											
TOM-197	0.707629	0.000003											
TOM-198	0.707338	0.000004											
TOM-199	0.707413	0.000002											
TOM-200	0.707522	0.000003	0.51246	0.000008	−3.44	19.1464	0.0010	15.6610	0.0008	38.9168	0.0020	2.485	0.818
TOM-201	0.707408	0.000003	0.51245	0.000009	−3.65	19.6331	0.0008	15.6537	0.0006	38.8605	0.0017	2.483	0.797
TOM-202	0.707320	0.000004				19.1079	0.0012	15.6688	0.0008	38.9102	0.0022	2.483	0.820
TOM-203	0.707572	0.000004											
HNK-1	0.707913	0.000005	0.51256	0.00001	−1.54	23.0776	0.0011	16.0106	0.0006	38.8026	0.0015	2.424	0.694
TOM-191	0.706988	0.000004	0.51245	0.00001	−3.70	26.8228	0.0015	16.4489	0.0009	39.0100	0.0026	2.372	0.613
TOM-192	0.707215	0.000006	0.51257	0.00001	−1.32	17.4536	0.0006	15.4647	0.0009	36.9404	0.0035	2.389	0.886
TOM-193	0.709125	0.000007	0.51256	0.00001	−1.51	19.5392	0.0014	15.7619	0.0010	38.8836	0.0025	2.467	0.807
TOM-194	0.708578	0.000007	0.51253	0.00001	−2.11	19.4558	0.0043	15.6897	0.0009	38.9625	0.0019	2.483	0.806
TOM-195	0.707841	0.000006	0.51251	0.00001	−2.45	19.1138	0.0005	15.6203	0.0005	39.1833	0.0016	2.508	0.817
TOP-1	0.707094	0.000004	0.51246	0.00001	−3.39	21.9279	0.0008	15.9379	0.0005	38.3260	0.0013	2.405	0.727
TOP-2	0.707076	0.000005	0.51246	0.00001	−3.44	22.2404	0.0010	15.9498	0.0003	38.5417	0.0009	2.416	0.717
TOP-3	0.706854	0.000006	0.51247	0.00001	−3.38	25.7976	0.0008	16.2747	0.0005	38.2563	0.0014	2.351	0.631
TOP-4	0.706935	0.000005	0.51253	0.00001	−2.12	20.9243	0.0008	15.8283	0.0004	38.4930	0.0011	2.432	0.756
TOP-6	0.707877	0.000006	0.51245	0.00001	−3.68	19.0261	0.0006	15.6662	0.0005	38.0838	0.0015	2.431	0.823
TOP-7	0.707085	0.000007	0.51258	0.00001	−1.19	19.7219	0.0005	15.6880	0.0005	38.9281	0.0016	2.481	0.795
TOP-8	0.707618	0.000007	0.51241	0.00001	−4.43	22.4560	0.0052	15.9207	0.0012	38.9655	0.0036	2.447	0.709
TOP-9	0.707547	0.000004	0.51248	0.00001	−3.07	19.9508	0.0007	15.6537	0.0009	38.7132	0.0039	2.473	0.785
TOP-10	0.707403	0.000004	0.51253	0.00001	−2.07	19.7673	0.0009	15.6104	0.0009	38.1659	0.0037	2.445	0.790
TOP-11	0.708313	0.000007	0.51249	0.00001	−2.99	23.7966	0.0007	15.9258	0.0006	37.6869	0.0023	2.366	0.669

Sample	$\frac{^{87}Sr}{^{86}Sr}$	+/– (1s)	$\frac{^{143}Nd}{^{144}Nd}$	+/– (1s)	ε_{Nd}	$\frac{^{206}Pb}{^{204}Pb}$	+/– (1s)	$\frac{^{207}Pb}{^{204}Pb}$	+/– (1s)	$\frac{^{208}Pb}{^{204}Pb}$	+/– (1s)	$\frac{^{208}Pb}{^{207}Pb}$	$\frac{^{207}Pb}{^{206}Pb}$
Dongola													
DET-1	0.707058	0.000004	0.51223	0.00005	−8.05	19.1645	0.0041	15.6841	0.0036	38.6090	0.0083	2.462	0.818
SEL-1	0.706857	0.000005	0.51252	0.00001	−2.24	18.4430	0.0010	15.6220	0.0009	38.2049	0.0021	2.446	0.847
SEL-2	0.706796	0.000004	0.51277	0.00003	2.52								
SEL-3	0.706777	0.000007											
SEL-4	0.706915	0.000004	0.51249	0.00002	−2.87	18.6480	0.0007	15.6362	0.0006	38.5473	0.0016	2.465	0.838
SEL-5	0.706874	0.000003	0.51273	0.00007	−1.75								
SEL-6	0.706946	0.000003	0.51254	0.00002	−1.93	19.2809	0.0005	15.7165	0.0004	38.7712	0.0012	2.467	0.815
SEL-7	0.707044	0.000004	0.51260	0.00001	−0.67	19.4456	0.0015	15.6803	0.0012	38.5600	0.0030	2.459	0.806
SEL-8	0.706932	0.000004	0.51268	0.00002	0.82	18.6187	0.0021	15.6225	0.0018	38.2388	0.0041	2.448	0.839
SEL-9	0.706764	0.000006				18.6306	0.0002	15.5809	0.0002	38.3593	0.0004	2.462	0.836
SEL-10	0.707284	0.000008	0.51246	0.00005	−3.40								
SEL-11	0.707334	0.000004	0.51276	0.00003	2.31								
SEL-12	0.706877	0.000006	0.51245	0.00001	−3.73								
SEL-13	0.706759	0.000005	0.51259	0.00003	−0.95	18.5602	0.001	15.6542	0.001	38.5413	0.0018	2.462	0.843
SEL-14	0.706633	0.000006	0.51246	0.00001	−3.41	19.1206	0.001	15.7006	0.001	38.5046	0.0014	2.452	0.821
SEB-1	0.707032	0.000006	0.51213	0.00010	−9.96	18.3889	0.0009	15.6276	0.0008	38.3942	0.0020	2.457	0.850
SEB-2	0.707056	0.000006				19.1729	0.0008	15.6793	0.0007	38.4547	0.0016	2.453	0.818
SEB-3	0.707308	0.000005				18.4357	0.0010	15.6321	0.0008	38.4788	0.0022	2.462	0.848
SEB-4	0.707125	0.000004	0.51252	0.00007	−2.34								
SEB-5	0.707054	0.000005	0.51236	0.00005	−5.44	19.3435	0.0008	15.7164	0.0007	38.4470	0.0016	2.446	0.813
SEB-6	0.707068	0.000005	0.51240	0.00006	−4.64	18.3146	0.0008	15.6302	0.0008	38.4390	0.0020	2.459	0.853
DON-1	0.707522	0.000003	0.51245	0.00001	−3.70	18.9126	0.0003	15.6374	0.0003	38.5467	0.0008	2.465	0.827
DON-2	0.707618	0.000004	0.51245	0.00001	−3.63	19.3794	0.0009	15.6764	0.0008	38.8132	0.0018	2.476	0.809
DON-3	0.708309	0.000005	0.51248	0.00001	−3.08	19.1902	0.0003	15.6667	0.0003	38.7797	0.0007	2.475	0.816
Shendi													
SRA-1	0.707852	0.000005	0.51247	0.00001	−3.37	18.7611	0.0014	15.6498	0.0011	38.6283	0.0027	2.468	0.834
SRA-2	0.708585	0.000005	0.51227	0.00001	−7.19	19.5457	0.0017	15.6614	0.0014	38.4201	0.0034	2.453	0.801
SRA-3	0.709170	0.000009	0.51225	0.00001	−7.57	19.1328	0.0014	15.6583	0.0012	38.6710	0.0030	2.470	0.818
SRA-4	0.707908	0.000008	0.51244	0.00001	−3.94								
SRA-5	0.707837	0.000003	0.51252	0.00001	−2.27								
SRA-6	0.707784	0.000007	0.51249	0.00002	−2.91	18.7758	0.0011	15.6323	0.0010	38.5338	0.0024	2.465	0.833
SRA-7	0.707790	0.000005	0.51260	0.00002	−0.72								
SRA-8	0.707704	0.000004	0.51256	0.00002	−1.60	18.6522	0.0008	15.6537	0.0007	38.6544	0.0019	2.469	0.839
Askut													
ASK-15	0.708787	0.000008	0.51254	0.00001	−1.94	18.2554	0.0007	15.6058	0.0006	38.1367	0.0014	2.444	0.855
ASK-16	0.707465	0.000004				19.5053	0.0015	15.6880	0.0007	38.7774	0.0020	2.472	0.804
ASK-17	0.707027	0.000007	0.51248	0.00001	−3.08	19.2550	0.0014	15.7001	0.0012	39.0670	0.0051	2.488	0.815
ASK-18	0.706736	0.000003	0.51253	0.00001	−2.11	19.3757	0.0011	15.6536	0.0007	38.9920	0.0017	2.491	0.808
ASK-19	0.709166	0.000009	0.51255	0.00001	−1.69	18.7436	0.0006	15.6461	0.0005	38.5875	0.0013	2.466	0.835
ASK-20	0.706749	0.000004	0.51251	0.00001	−2.46	19.1766	0.0006	15.6812	0.0005	38.7074	0.0013	2.468	0.818
ASK-21	0.706737	0.000006	0.51257	0.00002	−1.35	18.9056	0.0020	15.6610	0.0015	38.6198	0.0039	2.466	0.828
ASK-22	0.707646	0.000004	0.51248	0.00001	−3.03	19.0460	0.0015	15.6825	0.0013	38.7469	0.0031	2.471	0.823
ASK-23	0.706743	0.000005	0.51258	0.00001	−1.09	18.8380	0.0013	15.6858	0.0010	38.7734	0.0061	2.472	0.833
ASK-24	0.708245	0.000007	0.51254	0.00001	−1.89	18.9984	0.0015	15.6513	0.0010	38.6000	0.0022	2.466	0.824
ASK-25	0.709006	0.000010	0.51251	0.00001	−2.54	19.3744	0.0010	15.6670	0.0007	39.1115	0.0020	2.496	0.809
ASK-26	0.706692	0.000004	0.51253	0.00001	−2.12	19.3405	0.0005	15.6691	0.0004	39.0740	0.0011	2.494	0.810
ASK-27	0.707398	0.000003	0.51249	0.00001	−2.81	18.7765	0.0029	15.5397	0.0033	38.5106	0.0132	2.478	0.828
ASK-28	0.707221	0.000005				19.1169	0.0008	15.6429	0.0006	38.5833	0.0016	2.467	0.818
ASK-29	0.708287	0.000006	0.51247	0.00001	−3.33	18.9805	0.0067	15.6521	0.0010	38.7122	0.0023	2.473	0.825
ASK-30	0.706580	0.000005	0.51257	0.00001	−1.26	18.6738	0.0004	15.6290	0.0003	38.4083	0.0010	2.458	0.837
Abri													
ABR-1	0.707177	0.000005	0.51237	0.00001	−5.22	18.4623	0.0004	15.6317	0.0004	38.2031	0.0008	2.444	0.847
ABR-2	0.707371	0.000007	0.51232	0.00001	−6.27	18.4810	0.0003	15.6491	0.0003	38.1596	0.0008	2.438	0.847
ABR-3	0.707517	0.000020	0.51231	0.00001	−6.32	18.8454	0.0002	15.6621	0.0002	38.0855	0.0006	2.432	0.831
ABR-4	0.706891	0.000009	0.51237	0.00001	−5.26	18.6530	0.0003	15.6905	0.0002	38.3365	0.0006	2.443	0.841
Wadi Halfa													
WH-1	0.707678	0.000006	0.51225	0.00001	−7.56	18.5287	0.0003	15.6458	0.0003	38.1589	0.0007	2.439	0.844
WH-3	0.707806	0.000006	0.51226	0.00001	−7.45	19.6030	0.0003	15.7423	0.0002	38.0201	0.0006	2.415	0.803
WH-4	0.708056	0.000004	0.51224	0.00001	−7.85	18.5329	0.0003	15.6436	0.0002	38.2828	0.0005	2.447	0.844
WH-5	0.707885	0.000006				19.6977	0.0004	15.7342	0.0003	38.2016	0.0007	2.428	0.799
WH-6	0.707484	0.000004	0.51221	0.00001	−8.38	18.5664	0.0003	15.6459	0.0003	38.1562	0.0007	2.439	0.843
WH-7	0.707924	0.000007	0.51227	0.00001	−7.19	18.2320	0.0004	15.6202	0.0003	38.0895	0.0008	2.438	0.857
WH-8	0.708265	0.000006	0.51221	0.00001	−8.32	18.1230	0.0002	15.6113	0.0002	38.1281	0.0005	2.442	0.861
WH-9	0.707512	0.000008	0.51229	0.00001	−6.82	18.3763	0.0005	15.6329	0.0004	38.0458	0.0012	2.434	0.851
WH-10	0.708192	0.000008	0.51226	0.00001	−7.48	18.1733	0.0002	15.6169	0.0002	38.1024	0.0005	2.440	0.859
WH-11	0.707339	0.000003	0.51251	0.00001	−2.53	19.4187	0.0003	15.6849	0.0002	38.7396	0.0006	2.470	0.808

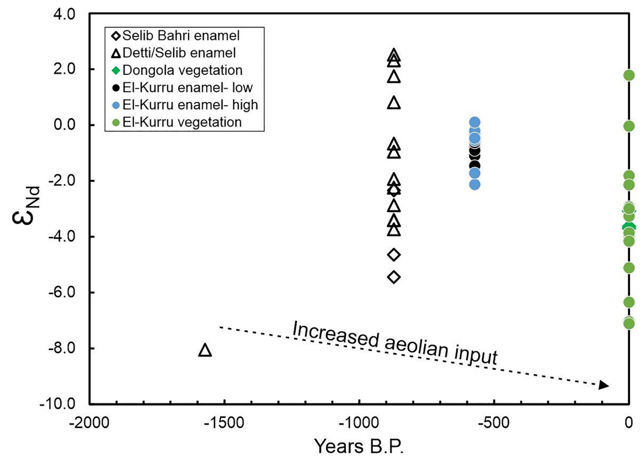

Figure 8. Time versus ε_{Nd} values for samples from the Dongola and El-Kurru regions of the NRVS. The Nd isotope data for human tooth enamel from these regions are not consistent with an expected trend of decreasing ε_{Nd} values with decreasing time. In general, the data illustrate increasing ε_{Nd} values towards present-day and complete overlap the range of Nd isotope compositions for present-day plants from the Dongola and El-Kurru regions. For the purposes of clarity, the age adopted for a suite of samples from an individual burial site shown here is illustrated as the midpoint based on the reported time period.

increase the variability of $^{87}Sr/^{86}Sr$ signatures for bioavailable Sr over time; however, this is clearly not the case based on the data depicted in Figure 7.

Figure 8 plots the ε_{Nd} values for enamel, faunal, and botanical samples from the Dongola and El-Kurru regions, and these data also provide support to the interpretations based on the Sr isotope data (i.e., if bioavailable Nd was impacted by increased aeolian contribution with decreasing age, then ε_{Nd} values should define negatively sloped trends in Figure 8). Materials of crustal origin are characterized by negative ε_{Nd} values as shown in Figures 3 and 4 (e.g., wadi riverine muds and Saharan dust). However, it is clear that this is not the case, and one may argue that the data shown in Figure 8 define the opposite trend of increasing ε_{Nd} values with decreasing age. Lastly, the same argument applies to the Pb isotope compositions reported here (Table 3; Figs. 5 and 6) since essentially none of the Pb isotope data, in particular for the tooth enamel, overlap those for Saharan dust (Figs. 5 and 6).

Conclusion

While it is not disputed that there was an increased aeolian contribution from the neighboring Sahara Desert as a result of drying climatic conditions during the Holocene within the NRVS, the new trace element and isotope data reported in this study clearly indicate that it did not impact the isotope record as preserved within human tooth enamel from archaeological sites of interest. Based on the Sr isotope compositions for human tooth enamel, faunal, and present-day botanical samples reported here, it is clear that these do not exhibit a systematic increase with decreasing age, as would be the expected temporal trend had the archaeological sites been impacted by increased contribution of Saharan dust. Overall, the Sr isotope compositions for human tooth enamel from the different time periods overlap those of their corresponding faunal samples, and in some instances that of much younger, present-day botanical samples from the same site (e.g., Tombos). Moreover, the Nd and Pb isotope data both corroborate the interpretations based on the Sr isotope ratios. The reasons for the lack of environmental impact may be several-fold: (1) The time required for elements such as Sr originating from aeolian dust to be incorporated within the ecological and hydrological cycles may exceed that of the archaeological record being investigated. In particular, if most of the Sr is bound in silicate minerals, it may be either more difficult to weather or metabolize compared to carbonate-hosted Sr; and/or (2) from a mass balance perspective, the relatively low abundances of Sr present within aeolian dust renders it ineffective in impacting the Sr isotopic composition of the local environment, which is characterized in general by much higher concentrations of Sr (e.g., soil sample NSO-1, Sr content = 419 ppm; Table 2). Hence, it can be concluded that Sr isotope compositions of non-altered archaeological human tooth enamel most likely reflect those of their local environment and can be used for provenance studies.

Acknowledgements

The archaeological remains used in this study were excavated and exported with the cooperation of the National Corporation of Antiquities and Museums in Sudan facilitated by El Tahir Adam Elnour and El Hassan Ahmed Mohamed. We thank the community of Tombos for their support of the Tombos Archaeological Project and their kindness during our seasons, and co-director Stuart Tyson Smith for his collaboration. Mohamed Faroug Ali and Remah Abdelrahim Kabashi Ahmed greatly assisted in the collecting of plant samples and logistical arrangements in Sudan. We are grateful to our contributors to this project including Abagail Breidenstein, Iwona Kozieradzka-Ogunmakin, Shayla Monroe, and their respective institutions and collaborators. Dr. Loretta Corcoran is thanked for her assistance in processing some of the samples within the MITERAC ICP-MS Facility at the University of Notre Dame. We greatly appreciate the constructive comments from three reviewers that have improved the manuscript.

Funding

This work was funded by the National Science Foundation (BCS grant #1916718) to A. Simonetti and M.R. Buzon. Funding for additional samples was supported by Purdue University College of Liberal Arts Global Research Synergy program grant to M.R. Buzon.

Declarations and Conflict of Interest

The authors declare that they have no conflict of interest.

References

Abdel-Rahman, ElShiekh M. 1993. Geochemical and geotectonic controls of the metallogenic evolution of selected ophiolite complexes from the Sudan. *Berliner Geowisschaftliche Abhandlungen* A145.

Abdelsalam, Mohamed G., Richard J. Stern, Peter Copeland, Elfadi M. Elfaki, Bushra Elhur, and Fathelrahman M. Ibrahim. 1998. The Neoproterozoic Keraf suture in NE Sudan: sinistral transpression along the eastern margin of west Gondwana. *The Journal of Geology* 106:133–148.

Abouchami, Wafa, Kerstin Näthe, Ashwini Kumar, Stephen J.G. Galer, Klaus Peter Jochum, Earle Williams, et al. 2013. Geochemical and isotopic characterization of the Bodélé Depression dust source and implications for transatlantic dust transport to the Amazon Basin. *Earth Planetary Science Letters* 380:112–123. DOI: 10.1016/j.epsl.2013.08.028.

Bailo, Eltahir, Heinz Schandelmeier, Gerhard Franz, Chih-Hsien Sun, and Richard J. Stern. 2003. Plutonic and metamorphic rocks from the Keraf Suture (NE Sudan): A glimpse of Neoproterozoic tectonic evolution on the NE margin of W. Gondwana. *Precambrian Research* 123:67–80. DOI: 10.1016/S0301–9268(03)00044-5.

Baker, Joel, David Peat, Tod Waight, and Christine Meyzen. 2004. Pb isotopic analysis of standards and samples using a 207Pb–204Pb double spike and thallium to correct for mass bias with a double-focusing MC-ICP-MS. *Chemical Geology* 211(3–4): 275–303. DOI: 10.1016/j.chemgeo.2004.06.030.

Balboni, Enrica, Nina Jones, Tyler Spano, Antonio Simonetti, and Peter C. Burns. 2016. Chemical and Sr isotopic characterization of North America uranium ores: nuclear forensic applications. *Applied Geochemistry* 74:24–32. DOI: 10.1016/j.apgeochem.2016.08.016.

Barbieri, Mario, Tatiana V. Kuznetsova, Vladimir I. Nikolaev, and Maria Rita Palombo. 2008. Strontium isotopic composition in late Pleistocene mammal bones from the Yakutian region (North-Eastern Siberia). *Quaternary International* 179:72–78. DOI: 10.1016/j.quaint.2007.08.014.

Barth, Henner, and Dieter K. Meinhold. 1979. Mineral prospecting in the Bayuda Desert. Part 1, Volume A. Investigation of mineral potential. *Technical Report Sudanese-German Exploration Project*. Bundesanstalt fur Geowissenschaften und Rohstoffe, Hannover.

Bataille, Clement P., Isabella C.C. von Holstein, Jason E. Laffoon, Matte Willmes, Xiao-Ming Liu, and Gareth R. Davies. 2018. A bioavailable strontium isoscape for Western Europe: A machine learning approach. *PLoS ONE* 13(5):0197386. DOI: 10.1371/journal.pone.0197386.

Bentley, R. Alexander. 2006. Strontium isotopes from the earth to the archaeological skeleton: A review. *Journal of Archaeological Method and Theory* 13(3):135–187. DOI: 10.1007/s10816-006-9009-x.

Buzon, Michele R., Antonio Simonetti, and Robert A. Creaser. 2007. Migration in the Nile Valley during the New Kingdom period: A preliminary strontium isotope study. *Journal of Archaeological Science* 34(9):1391–1401. DOI: 10.1016/j.jas.2006.10.029.

Buzon, Michele R., and Andrea Bombak. 2010. Dental disease in the Nile Valley during the New Kingdom. *International Journal of Osteoarchaeology* 20:371–387. DOI: 10.1002/oa.1054.

Buzon, Michele R., and Antonio Simonetti. 2013. Strontium isotope ($^{87}Sr/^{86}Sr$) variability in the Nile Valley: Identifying residential mobility during ancient Egyptian and Nubian sociopolitical changes in the New Kingdom and Napatan Periods. *American Journal of Physical Anthropology* 151(1):1–9. DOI: 10.1002/ajpa.22235.

Buzon, Michele R., Stuart Tyson Smith, and Antonio Simonetti. 2016. Entanglement and the formation of the ancient Nubian Napatan state. *American Anthropologist* 118(2):284–300. DOI: 10.1111/aman.12524.

Canadell, Josep, Robert B. Jackson, James R. Ehleringer, Harold A. Mooney, Osvaldo E. Sala, and Ernst Detlef Schulze. 1996. Maximum rooting depth of vegetation types at the global scale. *Oecologia* 108(4):583–595. DOI: 10.1007/BF00329030.

Capo, Rosemary C., Brian W. Stewart, and Oliver A. Chadwick. 1998. Strontium isotopes as tracers of ecosystem processes: theory and methods. *Geoderma* 82(1–3):197–225. DOI: 10.1016/S0016-7061(97)00102-X.

Chadwick, Oliver A., Louis A. Derry, Peter M. Vitousek, B.J. Huebert, and Lars O. Hedin. 1999. Changing sources of nutrients during four million years of ecosystem development. *Nature* 397:491–497.

Chester, Roy, Henry Elderfeld, John J. Griffin, L.R. Johnson, and R.C. Padgham. 1972. Eolian dust along the eastern margins of the Atlantic Ocean. *Marine Geology* 13(2):91–105. DOI: 10.1016/0025-3227(72)90048-5.

Coble, Ashley A., Stephen C. Hart, Michael E. Ketterer, Gregory S. Newman, and Andrew L. Kowler. 2015. Strontium source and depth of uptake shifts with substrate age in semiarid ecosystems. *Journal of Geophysical Research* 120(6):1069–1077. DOI: 10.1002/2015JG002992.

Dominy, Nathaniel J., Salima Ikram, Gillian L. Moritz, Patrick V. Wheatley, John N. Christensen, Jonathan W. Chipman, et al. 2020. Mummified baboons reveal the far reach of early Egyptian mariners. *Elife* 9:e60860. DOI: 10.7554/eLife.60860.

Ericson, Jonathon E. 1985. Strontium isotope characterization in the study of prehistoric human ecology. *Journal of Human Evolution* 14:503–514.

Evans, Christopher H. 1990. *Biochemistry of the Lanthanides*, Plenum Press, New York. DOI: 10.1007/978-1-4684-8748-0.

Evans, Jane, Vanessa Pashley, Carolyn A. Chenery, Louise Loe, and Simon R. Chenery. 2018. Lead isotope analysis of tooth enamel from a Viking age mass grave in southern Britain and the constraints it places on the origin of the individuals. *Archaeometry* 60:859–869. DOI: 10.1111/arcm.12361.

Evans, Jane, Nick Stoodley, and Carolyn Chenery. 2006. A strontium and oxygen isotope assessment of a possible fourth century immigrant population in a Hampshire cemetery, southern England. *Journal of Archaeological Science* 33:265–272. DOI: 10.1016/j.jas.2005.07.011.

Evuk, David, Gerhard Franz, Dirk Frei, and Friedrich Lucassen. 2014. The Neoproterozoic evolution of the central-eastern Bayuda Desert (Sudan). *Precambrian Research* 240:108–125. DOI: 10.1016/j.precamres.2013.10.015.

Evuk, David, Friedrich Lucassen, and Gerhard Franz. 2017. Lead isotope evolution across the Neoproterozoic boundary between craton and juvenile crust, Bayuda Desert, Sudan. *Journal of African Earth Sciences* 135:72–81. DOI: 10.1016/j.jafrearsci.2017.08.008.

Faure, Gunther. 1986. *Principles of Isotope Geology.* Wiley-Liss, New York.

Faure, Gunther, and Teresa M. Mensing. 2005. *Isotopes: Principles and Applications, third ed.* John Wiley and Sons, Inc., Hoboken, New Jersey.

Fielding, Laura. 2015. *A Multi-technique provenance study of the Oligocene recent Nile cone sediments and river Nile hinterland.* Ph.D. dissertation, Lancaster University. Proquest, University of Notre Dame, IN.

Frei, Karin M., and Robert Frei. 2011. The geographic distribution of strontium isotopes in Danish surface waters—A base for provenance studies in archaeology, hydrology and agriculture. *Applied Geochemistry* 26(3):326–340. DOI: 10.1016/j.apgeochem.2010.12.006.

Goldstein, Steven J., and Stein B. Jacobsen. 1987. The Nd and Sr isotopic systematics of river-water dissolved material: Implications for the sources of Nd and Sr in seawater. *Chemical Geology* 66:245–272. DOI: 10.1016/0168-9622(87)90045-5.

Goudie, Andrew S. 1983. Dust storms in space and time. *Progress in Physical Geography: Earth and Environment* 7:502–530. DOI: 10.1177/030913338300700402.

Goudie, Andrew S. 2008. The history and nature of wind erosion in deserts. *Annual Review of Earth and Planetary Sciences* 36:97–119. DOI: 10.1146/annurev.earth.36.031207.124353.

Goudie, Andrew S., and Nicholas J. Middleton. 2001. Saharan dust storms: Nature and consequences. *Earth-Science Reviews* 56:179-204. DOI: 10.1016/S0012-8252(01)00067-8.

Graustein, William C., and Richard L. Armstrong. 1983. The use of $^{87}Sr/^{86}Sr$ ratios to measure atmospheric transport into forested watersheds. *Science* 219:289–292. DOI: 10.1126/science.219.4582.289.

Graves, Carl. 2018. Intercultural Communication: Egypt and Nubia c. 2543–1076BC. Connections. University of Birmingham online exhibition catalogue. https://www.birmingham.ac.uk/research/activity/connections/Essays/CGraves.aspx, accessed October 29, 2018.

Gregoricka, Lesley A., and Brenda J. Baker. 2021. Residential mobility, pastoralism, and community in ancient Kush. Paper presented at the Meeting of the American Association of Physical Anthropologists, Baltimore, MD.

Guinoiseau, Damien, Satinder P. Singh, Stephen J.G. Galer, Wafa Abouchami, Rohan Bhattacharyya, Konrad Kandler, et al. 2022. Characterization of Saharan and Sahelian dust sources based on geochemical and radiogenic isotope signatures. *Quaternary Science Reviews* 293:107729. DOI: 10.1016/j.quascirev.2022.107729.

Hedges, Robert E.M., and Andrew R. Millard. 1995. Bones and groundwater: Towards the modeling of diagenetic processes. *Journal of Archaeological Science* 22:155–64.

Herrick, Hannah. 2018. Applying Sr Geoprovenance to anthropogenic charcoal: In theory & practice. In *Meeting of Frontiers in Archaeological Science 2*, Simon Fraser University, British Columbia.

Hillson, Simon. 1996. *Dental Anthropology.* Cambridge University Press, Cambridge. DOI: 10.1017/CBO9781139170697.

Hodell, David A., Rhonda L. Quinn, Mark Brenner, and George Kamenov. 2004. Spatial variation of strontium isotopes (Sr-87/Sr-86) in the Maya region: A tool for tracking ancient human migration. *Journal of Archaeological Science* 31(5):585–601. DOI: 10.1016/j.jas.2003.10.009.

Jackson, Robert B., Josep Canadell, James R. Ehleringer, Harold A. Mooney, Osvaldo E. Sala, and Ernst Detlef Schulze. 1996. A global analysis of root distributions for terrestrial biomes. *Oecologia* 108(3):389–411. DOI: 10.1007/BF00333714.

Jewell, Amy, Nick Drake, Anja J. Crocker, Natalie L. Bakker, Tereza Kunkelova, Charlie S. Bristow, et al. 2021. Three North African dust source areas and their geochemical fingerprint. *Earth and Planetary Science Letters* 554:116645. DOI: 10.1016/j.epsl.2020.116645.

Jung, Stefan J.A., Gareth R. Davies, Gerald M. Ganssen, and Dirk Kroon. 2004. Stepwise Holocene aridification in NE Africa deduced from dust-borne radiogenic isotope records. *Earth Planetary Science Letters* 221:27–37. DOI: 10.1016/S0012-821X(04)00095-0.

Kamenov, George D., Ellen M. Lofaro, Gennifer Goad, and John Krigbaum. 2018. Trace elements in modern and archaeological human teeth: Implications for human metal exposure and enamel diagenetic changes. *Journal of Archaeological Science* 99:27–34. DOI: 10.1016/j.jas.2018.09.002.

Kennedy, Martin J., Oliver A. Chadwick, Peter M. Vitousek, Louis A. Derry, and David M. Hendricks. 1998. Changing sources of base cations during ecosystem development, Hawaiian Islands. *Geology* 26:1015–1018.

Kieffer, Bruno, Nicholas Arndt, Henriette Lapierre, Florence Bastien, Delphine Bosch, Arnaud Pecher, et al. 2004. Flood and shield basalts from Ethiopia: magmas from the African superswell. *Journal of Petrology* 45:793–834. DOI: 10.1093/petrology/egg112.

Koeman, Elizabeth C., Antonio Simonetti, and Peter C. Burns. 2015. Sourcing of copper and lead within red inclusions from trinitite post detonation material. *Analytical Chemistry* 87:5380–5386. DOI: 10.1021/acs.analchem.5b00696.

Kohfeld, Karen E., and Sandy P. Harrison. 2001. DIRTMAP: the geological record of dust. *Earth-Science Reviews* 54:81–114.

Kohn, Matthew J., Margaret J. Schoeninger, and William W. Barker. 1999. Altered states: Effects of diagenesis on fossil tooth chemistry. *Geochimica et Cosmochimica Acta* 63:2737–2747.

Kozieradzka-Ogunmaki, Iwona. 2021. Isotope analysis and radiocarbon dating of human remains from El-Zuma. In *Early Makuria Research Project: El-Zuma Cemetery*, edited by M. El-Tayeb and E. Czyzewska-Zalewska, pp. 220–227. (Harvard Egyptological Studies; Vol. 13). Brill DOI: 10.1163/9789004433755_008.

Kulaksiz, Serkan, and Michael Bau. 2013. Anthropogenic dissolved and colloid/nanoparticle bound samarium, lanthanum and gadolinium in the Rhine River and the impending destruction of the natural rare earth element distribution in rivers. *Earth Planetary Science Letters* 362:43–50. DOI: 10.1016/j.epsl.2012.11.033.

Küster, Dirk, and Jean-Paul Liégeois. 2001. Sr, Nd isotopes and geochemistry of the Bayuda Desert high-grade metamorphic-basement (Sudan): An early Pan-African oceanic convergent margin, not the edge of the East Saharan ghost craton. *Precambrian Research* 109:1–23. DOI: 10.1016/S0301-9268(00)00147-9.

Küster, Dirk, Jean-Paul Liégeois, Dmitry Matukov, Sergei Sergeev, and Friedrich Lucassen. 2008. Zircon geochronology and Sr, Nd, Pb isotope geochemistry of granitoids from Bayuda Desert and Sabaloka (Sudan): Evidence for a Bayudian event (920-900 Ma) preceding the Pan-African orogenic cycle (860-590 Ma) at the eastern boundary of the Saharan Metacraton. *Precambrian Research* 164:16–39. DOI: 10.1016/j.precamres.2008.03.003.

Lahtinen, Maria, Laura Arppe, and Geoff Nowell. 2021. Source of strontium in archaeological mobility studies—marine diet contribution to the isotopic composition. *Archaeological and Anthropological Sciences* 13(1). DOI: 10.1007/s12520-020-01240-w.

Maher, Barbara A., Joseph M. Prospero, Doug Mackie, Diego Gaiero, Paul P. Hesse, and Yves Balkanski. 2010. Global

—-1
—0
—+1

connections between aeolian dust, climate and ocean biogeochemistry at the present day and at the last glacial maximum. *Earth-Science Reviews* 99:61–97. DOI: 10.1016/j.earscirev.2009.12.001.

Manhes, Gérard, Claude J. Allègre, Bernard Dupré, and Bruno Hamelin. 1980. Lead isotope study of basic ultrabasic layered complexes: Speculations about the age of the Earth and primitive mantle characteristics. *Earth Planetary Science Letters* 47(3):370–382. DOI: 10.1016/0012-821X(80)90024-2.

Maritan, Lara, Elisa Gravagna, Giancarlo Cavazzini, Andrea Zerboni, Claudio Mazzoli, Celestino Grifa, et al. (2021). Nile River clayey materials in Sudan: Chemical and isotope analysis as reference data for ancient pottery provenance studies. *Quaternary International*. DOI: 10.1016/j.quaint.2021.05.009.

Middleton, Nicholas J., and Andrew S. Goudie. 2001. Saharan dust: Source sand trajectories. *Transactions of the Institute of British Geographers* 26(2):165–181. DOI: 10.1111/1475-5661.00013.

Millard, Andrew, Janet Montgomery, Mark Trickett, Julia Beaumont, Jane Evans, and Simon Chenery. 2014. Childhood lead exposure in the British Isles during the Industrial Revolution. In *Modern Environments and Human Health: Revisiting the Second Epidemiologic Transition*, edited by M.K. Zuckerman, pp. 279–99, Wiley-Blackwell, Hoboken, NJ. DOI: 10.1002/9781118504338.ch15.

Miller, Eric K., Joel D. Blum, and Andrew J. Friedland. 1993. Determination of soil exchangeable-cation loss and weathering rates using Sr isotopes. *Nature* 362(6419):438–441.

Montgomery, Janet, Jane A. Evans, Simon R. Chenery, Vanessa Pashley, and Kristina Killgrove. 2010. "Gleaming, white and deadly": The use of lead to track human exposure and geographic origins in the Roman period in Britain. *Journal of Roman Archaeology Supplement* 78: 204–26.

Nelson, Bruce K., Michael J. Deniro, Margaret J. Schoeninger, Donald J. DePaolo, and Peter E. Hare. 1986. Effects of diagenesis on strontium, carbon, nitrogen, and oxygen concentration and isotopic concentration of bone. *Geochimica et Cosmochimica Acta* 50(9):1941–1949.

Nielsen-March, Christina M., and Robert E. M. Hedges. 2000. Patterns of diagenesis in bone II: Effects of acetic acid treatment and the removal of diagenetic $(CO_3)^{2-}$. *Journal of Archaeological Science* 27(12):1151–1159. DOI: 10.1006/jasc.1999.0538.

Osypinska, Marta, Piotr Osypinski, Zdzislaw Belka, Marek Chlodnicki, Paweł Wiktorowicz, Robert Ryndziewicz, et al. 2021. Wild and domestic cattle in the ancient Nile Valley: Marks of ecological change. *Journal of Field Archaeology* 46(7):429–447. DOI: 10.1080/00934690.2021.1924491.

Padoan, Marta, Eduardo Garzanti, Yehudit Harlavan, and Igor Maria Villa. 2011. Tracing Nile sediment sources by Sr and Nd isotope signatures (Uganda, Ethiopia, Sudan). *Geochimica et Cosmochimica Acta* 75(12):3627–3644. DOI: 10.1016/j.gca.2011.03.042.

Pietra, Romano, Enrico Sabbioni, L. Ubertalli, E. Orvini, G. Vocaturo, F. Colombo, et al. 1985. Trace elements in tissues of a worker affected by rare earths pneumoconiosis: A study carried out by neutron activation analysis, *Journal of Radioanalytical Nuclear Chemistry* 92:247–259. DOI: 10.1007/BF02219754.

Pik, Raphaël, Catherine Deniel, Christian Coulon, Gezahegn Yirgu, and Bernard Marty. 1999. Isotopic and trace element signatures of Ethiopian flood basalts: Evidence for plume-lithosphere interactions. *Geochimica et Cosmochimica Acta* 63(15):2263–2279. DOI: 10.1016/S0016-7037(99)00141-6.

Pik, Raphaël, Bernard Marty, Jean Carignan, Gezahegn Yirgu, and Teklewold Ayalew. 2008. Timing of East African Rift development in southern Ethiopia: Implication for mantle plume activity and evolution of topography. *Geology* 36(2):167–170. DOI: 10.1130/G24233A.1.

Plomp, Esther, Isabella C.C. von Holstein, Janne M. Koornneef, Richard J. Smeets, L. Font, J.A. Baart, et al. 2017. TIMS analysis of neodymium isotopes in human tooth enamel using 10^{13} Ω amplifiers. *Journal of Analytical Atomic Spectrometry* 32(12):2391–2400. DOI: 10.1039/c7ja00312a.

Plomp, Esther, Isabella C.C. von Holstein, Janne M. Koornneef, Richard J. Smeets, L. Font, J.A. Baart, et al. 2019. Evaluation of neodymium isotope analysis of human dental enamel as a provenance indicator using 10^{13} Ω amplifiers (TIMS). *Science & Justice* 59(3):322–331. DOI: 10.1016/j.scijus.2019.02.001.

Price, T. Douglas, James H. Burton, and R. Alexander Bentley. 2002. The characterization of biologically available strontium isotope ratios for the study of prehistoric migration. *Archaeometry* 44(1):117–135. DOI: 10.1111/1475-4754.00047.

Probst, Anne., A. El Gh'mari, Dominque Aubert, Bertrand Fritz, and Robert McNutt. 2000. Strontium as a tracer of weathering processes in a silicate catchment polluted by acid atmospheric inputs, Strengbach, France. *Chemical Geology* 170(1-4):203–219. DOI: 10.1016/S0009-2541(99)00248-X.

Prospero, Joseph M., Paul Ginoux, Omar Torres, Sharon E. Nicholson, and Thomas E. Gill. 2002. Environmental characterization of global sources of atmospheric soil dust identified with the Nimbus 7 Total Ozone Mapping Spectrometer (TOMS) absorbing aerosol product. *Reviews of Geophysics* 40(1):2-1-2-31. DOI: 10.1029/2000RG000095.

Pye, Kenneth. 2004. Isotope and trace element analysis of human teeth and bones for forensic purposes. *Geological Society of London Special Publications* 232:215–236. DOI: 10.1144/GSL.SP.2004.232.01.20.

Reinhardt, Eduard G., Daniel J. Stanley, and R. Timothy Patterson. 1998. Strontium isotopic paleontological method as a high-resolution paleosalinity tool for lagoonal environments. *Geology* 26:1003–1006.

Retzmann, Anika, Julia Budka, Helmut Sattmann, Johanna Irrgeher, and Thomas Prohaska. 2019. The New Kingdom population on Sai Island: Application of Sr isotopes to investigate cultural entanglement in Ancient Nubia. *Ägypten und Levante/Egypt and the Levant* 29:355–380. DOI: 10.1553/AEundL29s354.

Ruffer, Armand. 1920. Study of abnormalities and pathology of ancient Egyptian teeth. American *Journal of Physical Anthropology* 3(3):335–382. DOI: 10.1002/ajpa.1330030302.

Said, Rushdi. 1962. *The Geology of Egypt*. Elsevier, Amsterdam.

Samuel, Delwen. 1993. Ancient Egyptian bread and beer: An interdisciplinary approach. In *Biological Anthropology and the Study of Ancient Egypt*, edited by W. Vivian Davies and Roxi Walker, pp. 156–164. British Museum, London.

Schrader, Sarah A., Michele R. Buzon, Loretta Corcoran, and Antonio Simonetti. 2019. Intraregional $^{87}Sr/^{86}Sr$ variation in Nubia: New insights from the third cataract. *Journal of Archaeological Science Reports* 24:373–379. DOI: 10.1016/j.jasrep.2019.01.023.

Shin, Woo-Jin, Mukesh Kumar Gautam, Ji-Yu Shim, Han-Seul Lee, Sanghee Park, and Kwang-Sik Lee. 2022. Spatial distributions of strontium isotope ratios in human hair and tap water from South Korea. *Science of the Total Environment* 806:151352. DOI: 10.1016/j.scitotenv.2021.151352

Sillen, Andrew, Grant Hall, Stephen Richardson, and Richard Armstrong. 1998. $^{87}Sr/^{86}Sr$ ratios in modern and fossil food-webs of the Sterkfontein Valley: Implications for early hominid habitat preference. *Geochimica et Cosmochimica Acta* 62:2463–2473. DOI: 10.1016/S0016-7037(98)00182-3.

Simonetti, Antonio, Clément Gariépy, Catharine M. Banic, Richard Tanabe, and Henry K. Wong. 2004. Pb isotopic investigation of aircraft-sampled emissions from the Horne smelter (Rouyn, Quebec): Implications for atmospheric pollution in northeastern North America. *Geochimica et Cosmochimica Acta* 68:3285–3294. DOI: 10.1016/j.gca.2004.02.008.

Simonetti, Antonio, Michele R. Buzon, Loretta Corcoran, Abagail M. Breidenstein, and Geoff Emberling. 2021. Trace element and Pb and Sr isotope investigation of tooth enamel from archaeological remains at El-Kurru, Sudan: Evaluating the role of groundwater-related diagenetic alteration. *Applied Geochemistry* 132:105068. DOI: 10.1016/j.apgeochem.2021.105068.

Smith, Stuart Tyson. 1998. Nubia and Egypt: Interaction, acculturation, and secondary state formation from the third to first millennium B.C. In *Studies in Culture Contact: Interaction, Culture Change and Archaeology*, edited by James G. Cusick, pp. 256–287. Southern Illinois University, Carbondale.

Stantis, Chris, Arwa Kharobi, Nina Maaranen, Geoff M. Nowell, Manfred Bietak, Silvia Prell, et al. 2020. Who were the Hyksos? Challenging traditional narratives using strontium isotope ($^{87}Sr/^{86}Sr$) analysis of human remains from ancient Egypt. *PLoS ONE* 15(7):e0235414. DOI: 10.1371/journal.pone.0235414.

Stantis, Chris, Arwa Kharobi, Nina Maaranen, Colin Macpherson, Manfred Bietak, Silvia Prell, et al. 2021. Multi-isotopic study of diet and mobility in the northeastern Nile Delta. 2021. *Archaeological and Anthropological Sciences* 13:105. DOI: 10.1007/s12520-021-01344-x.

Stewart, Brian W., Rosemary C. Capo, and Oliver A. Chadwick. 1998. Quantitative strontium isotope models for weathering, pedogenesis and biogeochemical cycling. *Geoderma* 82(1-3): 173–195. DOI: 10.1016/S0016-7061(97)00101-8.

Tanaka, Tsuyoshi, Shigeko Togashi, Hikari Kamioka, Hiroshi Amakawa, Hiroo Kagami, Takuji Hamamoto, et al. 2000. JNdi-1: A neodymium isotopic reference in consistency with LaJolla neodymium. *Chemical Geology* 168:279–281.

Touzeau, Alexandra, Janne Blichert-Toft, Romain Amiot, François Fourel, François Martineau, Jenefer Cockitt, et al. 2013. Egyptian mummies record increasing aridity in the Nile Valley from 5500 to 1500 yr before present. *Earth Planetary Science Letters* 375(1):92–100. DOI: 10.1016/j.epsl.2013.05.014

Turner, Bethany L., George D. Kamenov, John D. Kingston, and George J. Armelagos. 2009. Insights into immigration and social class at Machu Picchu, Peru based on oxygen, strontium, and lead isotopic analysis. *Journal of Archaeological Science* 36(2):317–332. DOI: 10.1016/j.jas.2008.09.018.

Tütken, Thomas, Torsten W. Vennemann, and Hans-U Pfretzschner. 2011. Nd and Sr isotope compositions in modern and fossil bones: Proxies for vertebrate provenance and taphonomy. *Geochimica et Cosmochimica Acta* 75(20):5951–5970. DOI: 10.1016/j.gca.2011.07.024.

Tyler, Germund. 2004. Rare earth elements in soil and plant systems: A review. *Plant Soil* 267:191–206. DOI: 10.1007/s11104-005-4888-2.

Van der Hoven, Stephen J., and Jay Quade. 2002. Tracing spatial and temporal variations in the sources of calcium in pedogenic carbonates in a semiarid environment. *Geoderma* 108(3–4): 259–276. DOI: 10.1016/S0016-7061(02)00134-9.

Vitousek, Peter M., Martin J. Kennedy, Louis A. Derry, and Oliver A. Chadwick. 1999. Weathering versus atmospheric sources of strontium in ecosystems on young volcanic soils. *Oecologia* 121(2):255–259.

Washington, Richard, Martin Todd, Nicholas J. Middleton, and Andrew S. Goudie. 2003. Dust-storm source areas determined by the total ozone monitoring spectrometer and surface observations. *Annals of the Association of American Geographers* 93(2):297–313. DOI: 10.1111/1467-8306.9302003.

Weber, Michael, Théo Tacail, Federico Lugli, Marcus Clauss, Katrin Weber, Jennifer Leichliter, et al. 2020. Strontium uptake and intra-population $^{87}sr/^{86}sr$ variability of bones and teeth—controlled feeding experiments with rodents (Rattus norvegicus, Cavia porcellus). *Frontiers in Ecology and Evolution* 8:569940. DOI: 10.3389/fevo.2020.569940.

Whipkey, C.E., Rosemary C. Capo, Oliver A. Chadwick, and Brian W. Stewart. 2000. The importance of sea spray to the cation budget of a coastal Hawaiian soil: A strontium isotope approach. *Chemical Geology* 168(1-2):37–48. DOI: 10.1016/S0009-2541(00)00187-X.

Williams, Martin. 2019. Geology and soils. In *The Nile Basin: Quaternary Geology, Geomorphology and Prehistoric Environments*, edited by Martin Williams (pp. 33–58). Cambridge: Cambridge University Press. DOI: 10.1017/9781316831885.005.

Wong, Megan, Vaughan Grimes, Martin Steskal, Justin Song, John Ng, Klervia Jaouen, et al. 2021. A bioavailable baseline strontium isotope map of southwestern Turkey for mobility studies. *Journal of Archaeological Science: Reports* 37(7):102922. DOI: 10.1016/j.jasrep.2021.102922.

Woodward, Jamie, Mark Macklin, Laura Fielding, Ian Millar, Neal Spencer, Derek Welsby, et al. 2015. Shifting sediment sources in the world's longest river: A strontium isotope record for the Holocene Nile. *Quaternary Science Reviews* 130:124–140. DOI: 10.1016/j.quascirev.2015.10.040.

Zakrzewski, Sonia R., Andrew Shortland, and Joanne Rowland. 2016. *Science in the Study of Ancient Egypt*. Routledge, New York.

Supplementary Information

Table S1. Description of enamel and faunal samples investigated in this study.

Sample #	Site	Type	Tooth	Burial/Skeleton Info.	DATE
KUR-1	El-Kurru	Human	P	KU107	Christian
KUR-2	El-Kurru	Human	LM1	213	Christian
KUR-3	El-Kurru	Human	LP^2	104	Christian
KUR-4	El-Kurru	Human	RP_2	113	Christian
KUR-5	El-Kurru	Human	P	106	Christian
KUR-6	El-Kurru	Human	P_1	109	Christian
KUR-7	El-Kurru	Human	P	205	Christian
KUR-8	El-Kurru	Human	P	203	Christian
KUR-9	El-Kurru	Human	LP^1	206	Christian
KUR-10	El-Kurru	Human	RP_1	204	Christian
KUR-11	El-Kurru	Human	RP_2	270	Christian
KUR-12	El-Kurru	Human	ldm_1	211	Christian
KUR-13	El-Kurru	Human	LM^1	202	Christian
KUR-14	El-Kurru	Human	RM_3	110	Christian
KUR-15	El-Kurru	Human	RP	215	Christian
KUR-16	El-Kurru	Human	ldm_1	212	Christian
KUR-17	El-Kurru	Human	LPM_1	209	Christian
KUR-18	El-Kurru	Human	ldm1	214	Christian
NUF-1	Nuri	Tooth faunal		MD7:10-1	400 B.C.—240 A.D.
NUF-2	Nuri	Tooth faunal		MD7:10-2	400 B.C.—240 A.D.
NUF-3	Nuri	Tooth faunal		503-5	400 B.C.—240 A.D.
NUF-4	Nuri	Faunal tooth fill grave		F20	400 B.C.—240 A.D.
NUF-5	Nuri	Tooth faunal, poss. Camel		505-24	400 B.C.—240 A.D.
NSO-1	Nuri	Soil		Soil Sample	Present-day
HNK-1	Hannek	sheep/goat bone		264/F362	New Kingdom
TOM-191	Tombos	sus scrofa bone		U20L1/F445	New Kingdom
TOM-192	Tombos	sheep/goat bone		U20L2/F476	New Kingdom
TOM-193	Tombos	sheep/goat bone		U20L3/F502	New Kingdom
TOM-194	Tombos	leporid bone		U47S1L14/F558	New Kingdom
TOM-195	Tombos	faunal bone		U47S1L14/F559	New Kingdom
TOM-196	Tombos	Human	LP_4	U57PitB/BUr1	3rd Int. Period
TOM-197	Tombos	Human	RP^4	U57PitB/Iso. Cran.	3rd Int. Period
TOM-198	Tombos	Human	LP_4	U57PitB/ Bur2	3rd Int. Period
TOM-199	Tombos	Human	RP_4	U51L3/Bur1	3rd Int. Period
TOM-200	Tombos	Human	RM_1	U50L4/Bur1	3rd Int. Period
TOM-201	Tombos	Human	LP^3	U52/Bur1	3rd Int. Period
TOM-202	Tombos	Human	RP_3	U52/Bur2	3rd Int. Period
TOM-203	Tombos	Human	RP^4	U55L4	3rd Int. Period
DET-1	El-Detti	Human	RM2	T4	350–550 A.D.
SEL-1	Selib 1	Human	RM^1	SK1	1100–1200 A.D.
SEL-2	Selib 1	Human	LM_3	SK4	1100–1200 A.D.
SEL-3	Selib 1	Human	RM^3	SK6	1100–1200 A.D.
SEL-4	Selib 1	Human	LM_1	G2/SK3	1100–1200 A.D.
SEL-5	Selib 1	Human	LM^3	G3/SK8	1100–1200 A.D.
SEL-6	Selib 1	Human	RM^3	G5/SK6	1100–1200 A.D.
SEL-7	Selib 1	Human	LM_3	G11/SK2	1100–1200 A.D.
SEL-8	Selib 1	Human	LM_1	G14/SK7	1100–1200 A.D.
SEL-9	Selib 1	Human	LM^1	G24/SK5	1100–1200 A.D.
SEL-10	Selib 1	Human	premolar	G_E/SK1	1100–1200 A.D.
SEL-11	Selib 1	Human	LM^3	G_E/SK2	1100–1200 A.D.
SEL-12	Selib 1	Human	RM_1	SK1/2012	1100–1200 A.D.
SEL-13	Selib 1	Human	LM_3	SK2/2012	1100–1200 A.D.
SEL-14	Selib 1	Human	LM_3	SK5/2012	1100–1200 A.D.
SEB-1	Selib Bahri	Human	LM_2	G1/A	1100–1200 A.D.
SEB-2	Selib Bahri	Human	RM_2	G1/B	1100–1200 A.D.
SEB-3	Selib Bahri	Human	LM_2	G1/C	1100–1200 A.D.
SEB-4	Selib Bahri	Human	RM^3	G1/D	1100–1200 A.D.
SEB-5	Selib Bahri	Human	RP^1	G1/E	1100–1200 A.D.
SEB-6	Selib Bahri	Human	LM_2	G4	1100–1200 A.D.
SRA-1	Shendi/SRAP	Human	RM_2	T.5	400 B.C.–240 A.D.
SRA-2	Shendi/SRAP	Human	LM_3	T.10	400 B.C.–240 A.D.
SRA-3	Shendi/SRAP	Human	RM^3	T.11	400 B.C.–240 A.D.
SRA-4	Shendi/SRAP	Human	molar	T.12	400 B.C.–240 A.D.

Sample #	Site	Type	Tooth	Burial/Skeleton Info.	DATE
SRA-5	Shendi/SRAP	Human	LM_2	T.14	400 B.C.–240 A.D.
SRA-6	Shendi/SRAP	Human	RM^3	T.17	400 B.C.–240 A.D.
SRA-7	Shendi/SRAP	Human	LM_3	T.21-B	400 B.C.–240 A.D.
SRA-8	Shendi/SRAP	Human	Molar Lower	T.22	400 B.C.–240 A.D.
ASK-15	Askut	sheep/goat tooth		814	Middle Kingdom
ASK-16	Askut	sheep/goat tooth		945	Middle Kingdom
ASK-17	Askut	sheep/goat tooth		1220	Middle Kingdom
ASK-18	Askut	sheep/goat tooth		1224	Middle Kingdom
ASK-19	Askut	sheep/goat tooth		821	New Kingdom
ASK-20	Askut	sheep/goat tooth		892	New Kingdom
ASK-21	Askut	sheep/goat tooth		853	New Kingdom
ASK-22	Askut	sheep/goat tooth		1992	New Kingdom
ASK-23	Askut	sheep/goat tooth		1187	New Kingdom
ASK-24	Askut	sheep/goat tooth		1463	New Kingdom
ASK-25	Askut	hippo tusk (dentine)		842	New Kingdom
ASK-26	Askut	hippo tusk (dentine)		843	New Kingdom
ASK-27	Askut	sheep/goat tooth		1775	2nd Int. Period
ASK-28	Askut	sheep/goat tooth		1251	2nd Int. Period
ASK-29	Askut	sheep/goat tooth		1246	2nd Int. Period
ASK-30	Askut	Soil		1163	Middle Kingdom
ABR-4	Abri	Soil			Present-day
WH-11	Wadi Halfa	Soil			Present-day

Table S2. Chronology adapted from Smith (1998).

Date B.C.	Egypt (Dynasty)	Lower Nubia	Upper Nubia
3500–2600	Predynastic/Early Dynastic (1–3)	A-Group	Neolithic
2600–2150	Old Kingdom (4–6)	uncertain	Old Kerma
2150–2050	1st Intermediate Period (8–11)	C-Group	Old Kerma
2050–1650	Middle Kingdom (11–13)	C-Group	Middle Kerma
1650–1550	2nd Intermediate Period (14–17)	C-Group	Classic Kerma
1550–1050	New Kingdom (18–20)	C-Group	Recent Kerma
1050–750	3rd Intermediate Period (21–24)	uncertain	Pre-Napata
750–300	Late Period (25–30)	Napata	Napata
300 B.C.–400 A.D.	Greco-Roman	Meroitic	Meriotic